

Accepted Manuscript

The accumulation of Ni in serpentines and garnierites from the Falcondo Ni-laterite deposit (Dominican Republic) elucidated by means of μ XAS

Josep Roqué-Rosell, Cristina Villanova-de-Benavent, Joaquín A. Proenza

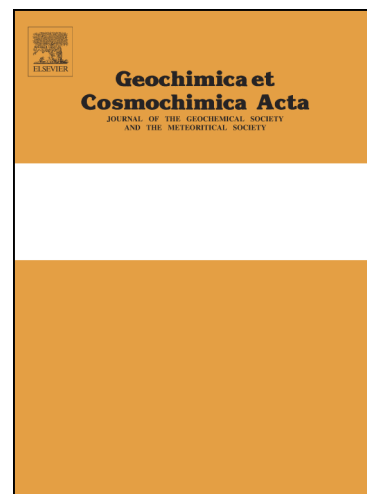
PII: S0016-7037(16)30641-X
DOI: <http://dx.doi.org/10.1016/j.gca.2016.11.004>
Reference: GCA 10007

To appear in: *Geochimica et Cosmochimica Acta*

Received Date: 9 October 2015
Revised Date: 1 November 2016
Accepted Date: 5 November 2016

Please cite this article as: Roqué-Rosell, J., Villanova-de-Benavent, C., Proenza, J.A., The accumulation of Ni in serpentines and garnierites from the Falcondo Ni-laterite deposit (Dominican Republic) elucidated by means of μ XAS, *Geochimica et Cosmochimica Acta* (2016), doi: <http://dx.doi.org/10.1016/j.gca.2016.11.004>

This is a PDF file of an unedited manuscript that has been accepted for publication. As a service to our customers we are providing this early version of the manuscript. The manuscript will undergo copyediting, typesetting, and review of the resulting proof before it is published in its final form. Please note that during the production process errors may be discovered which could affect the content, and all legal disclaimers that apply to the journal pertain.



**The accumulation of Ni in serpentines and garnierites from the Falcondo Ni-laterite deposit
(Dominican Republic) elucidated by means of μ XAS**

Josep Roqué-Rosell^a, Cristina Villanova-de-Benavent^a and Joaquín A. Proenza^a

^aDepartament de Mineralogia, Petrologia i Geologia Aplicada, Facultat de Geologia, Universitat de Barcelona, Martí i Franquès s/n, 08028 Barcelona, Catalonia, Spain

Corresponding author's contact:

Josep Roqué-Rosell; e-mail: josep.roque@ub.edu; Telephone: +(34)934021357; Fax: +(34)934021340

Abstract:

Ni-bearing serpentines and garnierites (Ni-bearing Mg-phyllsilicates) are the main Ni ores in the Falcondo Ni-laterite deposit (Dominican Republic). In the present paper a set of garnierite samples and the associated Ni-bearing serpentines with characteristic mineral compositions and textures, from the saprolite horizon, were studied by EMPA, μ XRF and μ XAS. The ultimate goal is to elucidate, for the first time, the Fe speciation and the Ni local environment of saprolite ores from Ni-laterites of the Dominican Republic. The chemical composition of the minerals has been obtained by means of EMPA and the Ni, Fe and Cr elemental maps obtained by μ XRF allowed distinguishing the saprolite fragments containing Ni-bearing serpentines and Fe oxyhydroxides from the garnierite veins. The Fe K-edge μ XANES demonstrated that Fe in the Ni-poor primary serpentine is mostly in the Fe²⁺ form, whereas in the Ni-bearing serpentine constituting the bulk of the saprolite and in the Fe-bearing garnierite Type I Fe was in the form of Fe³⁺. In parallel, the local environment of Ni determined by means of Ni K-edge μ EXAFS confirmed that in Ni-poor primary serpentines Ni formed a homogeneous Ni-Mg solid solution, in garnierites formed Ni-Ni clusters, and in Ni-bearing secondary serpentines Ni was found in Ni-Mg and Ni-Ni mixed sites. This paper explains the accumulation of Ni, the speciation of Fe in garnierites with various mineral compositions and in Ni-bearing serpentines from the saprolite horizon in Ni-laterite deposits.

1. Introduction

Lateritic nickel deposits are regoliths formed as a result of chemical weathering of ultramafic rocks (e.g. Freyssinet et al., 2005 and Butt and Cluzel, 2013). Under high temperatures and intense precipitations, the most soluble elements from the parent rock-forming minerals are leached. This results in the removal of Si and Mg and the accumulation of the less mobile elements (Elias, 2002, Freyssinet et al., 2005, Golightly, 1981, 2010). During this process, laterites develop two main horizons over the serpentinized peridotite protolith, a saprolite zone (consisting mostly of Ni-bearing serpentines and garnierite) and a limonite zone (formed by Fe-oxyhydroxides), which may be covered by ferricrete.

The Ni-laterites host over 60% of the world's land-based Ni resources (Gleeson et al., 2003 and Kuck, 2013), and the amount of Ni being extracted from laterite ores is increasing steadily (Mudd, 2010). It is estimated that about 10% of the world's Ni resources are found in the Caribbean region, and the Falcondo deposit is one of the largest hydrous Mg silicate-type Ni-laterite in the Caribbean, with estimated Ni reserves of about 79.2 million dry tons at a grade of 1.3 wt.% Ni (Falcondo Annual Report, 2010: http://www.falcondo.com.do/ES/Publicaciones/brochures/Memoria_FALCONDO_2010.pdf). In addition to its economic importance, Falcondo is an open air laboratory and allows a unique opportunity to study the weathering processes in laterites (Aiglsperger et al., 2015, 2016, Villanova-de-Benavent et al., 2014, 2016).

In Falcondo the main ores are the Ni-bearing serpentines and the garnierites from the saprolite horizon, the latter being the ones with highest Ni grades (e.g. Villanova-de-Benavent et al., 2014). During weathering, Ni present in the limonite horizon is simultaneously leached by meteoric solutions, is incorporated in the serpentines from the saprolite and is precipitated as garnierites in open fractures across the saprolite horizon. The term garnierite is a widely used field term to refer to the group of green, fine-grained, poorly crystallized, often intimately mixed nickel bearing magnesium phyllosilicates (e.g. Brindley & Hang, 1973, Springer, 1974, Brindley, 1978, Villanova-de-Benavent et al., 2014). In the Falcondo Ni-laterite, these phyllosilicates include the Mg-Ni series lizardite-népoite and chrysotile-pecoraite (serpentine group minerals with the composition $(\text{Mg,Ni})_3\text{Si}_2\text{O}_5(\text{OH})_4$), kerolite-pimelite (invalid names for hydrated talc-like phases with the formula $(\text{Mg,Ni})_3\text{Si}_4\text{O}_{10}(\text{OH})_2 \cdot n(\text{H}_2\text{O})$) and sepiolite-falcondoite $(\text{Mg,Ni})_4\text{Si}_6\text{O}_{15}(\text{OH})_2 \cdot 6(\text{H}_2\text{O})$).

The garnierites in the Falcondo Ni-laterite deposit display various shades of green which, in addition to their characteristic mineralogy, textural features and chemical composition, have been used to classify them into five groups (Villanova-de-Benavent et al., 2014, 2016). In addition, the secondary Ni-bearing precipitation sequence was established with the serpentine minerals developing first, followed by the precipitation of the talc-like phase, subsequent formation of the sepiolite-falcondoite series and, finally, Ni-free sepiolite and quartz (Galí et al., 2012). This well established sequence of garnierite precipitation in Falcondo provides a unique framework to study the Ni geochemistry and the Ni-serpentine and garnierite development in Ni-laterites.

Early synchrotron radiation studies by Manceau and coauthors dealt with the distribution of nickel in Ni-bearing Mg-phyllosilicates from New Caledonia (Manceau et al., 1985, Manceau and Calas, 1985, 1986). The EXAFS measurements on minerals of the lizardite-népoite and kerolite-pimelite

series indicate that the intracrystalline distribution of Ni within the phyllosilicates is not forming a homogeneous Ni-Mg solid solution but is segregated into discrete domains or clusters (Manceau and Calas, 1985). This work also pointed out that the Ni distribution within lizardite-népouite was probably derived from the transformation of earlier serpentines by a Ni-enrichment and a subsequent loss of Mg. However, in the case of kerolite-pimelite the work suggests that Ni heterogeneity takes place when these phases precipitate from an aqueous solution. More recently, Fan and Gerson (2011) and Dublet et al. (2012) discussed the distribution of Ni across a laterite profile and the incorporation of Ni in Ni-phyllosilicates in laterites from the Philippines and New Caledonia, respectively.

The results from Dublet et al. (2012) indicated that Ni accumulation across the laterite profile was mainly driven by the different weathering stages involved in the lateritization process. Dublet et al. (2012) demonstrated that Fe-oxihydroxides (mainly goethite) accumulated Ni at the most advanced stages of weathering within the limonitic horizon and that phyllosilicates (mainly serpentine) accumulated Ni within the saprolite horizon. In the study, the EXAFS analysis indicated that the intracrystalline distribution of Ni within the secondary, Ni-rich serpentine from the saprolite did not form a homogeneous Ni-Mg solid solution but was clustered into discrete domains (Dublet et al., 2012).

Nevertheless, there are still missing gaps in the study of Ni in Ni-bearing phyllosilicates. Up to now most of the XAS work has been done by means of bulk analysis on serpentine- and talc-like garnierite samples (Manceau et al., 1985, 1986, Manceau and Calas, 1985, Decarreau, 1992), with no data on sepiolite-like garnierites; or across several meters of a laterite profile (e.g. Fan and Gerson, 2011 and Dublet et al., 2012), without taking into account the garnierite mineralogy and textures, and their relationship with the host saprolite. In addition, the aforementioned literature focuses on Ni, and the distribution and speciation of Fe in this environment has not been studied. The Ni-laterites from the Caribbean region have been widely studied recently (Lewis et al. 2006, Tauler et al., 2009, Roqué-Rosell et al., 2010, Galí et al., 2012, Villanova-de-Benavent et al., 2014, 2016, Aiglsperger et al., 2015, 2016), however the present work is the first study of the Fe speciation and the Ni local environment by means of μ XAS in Caribbean saprolite ores.

In the present work, a set of samples containing Ni-bearing serpentines and garnierites was studied in an attempt to correlate their mineral composition and textures with the Ni enrichment that takes place during the lateritization in the Falcondo deposit. Initially a representative sample from each garnierite type was selected and characterized by means of optical microscopy (OM). Subsequently, the chemical compositions were obtained and the mineral phases were identified by means of electron microprobe analysis (EMPA) and micro X-ray fluorescence (μ XRF). Then, representative points of interest were defined within these regions, and synchrotron radiation microfocus X-ray absorption spectroscopy (μ XAS) was used in order to acquire Fe K-edge micro X-ray absorption near edge structure (μ XANES) and the Ni K-edge micro Extended X-Ray Absorption Fine Structure (μ EXAFS). The μ XAS measurements were used to quantify the oxidation state of Fe, identify the Fe-bearing minerals present and to elucidate the local environment of Ni within the phyllosilicates constituting the garnierites and serpentines of the saprolite.

The results from each technique were combined to present a picture of the mineralogy and the Ni accumulation and the Fe speciation in Ni-bearing serpentines and garnierites at Falcondo. Thus, the aim of this contribution is to understand the Ni crystal chemistry and the redox state of Fe in Ni-bearing serpentines and garnierites with the ultimate goal to achieve a better understanding on

the supergene enrichment of Ni in laterite profiles. This paper highlights the importance of the application of μ XAS in ore deposits and provides for the first time a detailed μ XAS study of garnierite formation in the Caribbean Ni-laterites.

2. Materials and methods

2.1. Sampling

In the present work, five samples from the saprolite horizon exposed in the mining pit of the Falcondo Ni-laterite deposit were selected (**Fig. 1**). These samples are thought to be the most representative from each one of the five garnierite types described and studied in detail by Villanova-de-Benavent et al. (2014, 2016). Samples L101A (type I), LC100B (type II), GAR2C (type III) and GAR6C (type IV) consist of saprolite fragments crosscut by millimeter to centimeter thick garnierite veins (**Fig. 1a-d**) and sample FALC3 (type V) represent massive garnierite aggregates (**Fig. 1e**).

2.2. Optical microscopy (OM)

Polished thin sections of the selected samples were studied by means of optical microscopy with plane polarized light. The OM was used to characterize the mineral textures and to select the representative regions of interest (ROI) to be studied in the samples by means of EMPA and μ XAS. On **Fig.1** each ROI contains one of the five garnierite types described in Villanova-de-Benavent et al. (2014) with the respective associated mineral assemblage, including fragments of weathered, serpentinized peridotite, garnierite veins and quartz crystals.

2.3. Electron Microprobe Analysis (EMPA)

The polished thin sections were analyzed by EMPA using a Cameca SX-50 at the Centres Científics i Tecnològics of the Universitat de Barcelona. The measurement conditions were 20 kV, at 15 nA probe current, a spot size of ca. 2 μ m, and a counting time of 20 s per element. The calibration standards used were: hematite (Fe, LIF, $K\alpha$), rutile (Ti, PET, $K\alpha$), periclase (Mg, TAP, $K\alpha$), rhodonite (Mn, LIF, $K\alpha$), Al_2O_3 (Al, TAP, $K\alpha$), Cr_2O_3 (Cr, PET, $K\alpha$), diopside (Si, TAP, $K\alpha$), NiO (Ni, LIF, $K\alpha$) and wollastonite (Ca, PET, $K\alpha$), metallic vanadium (V, LIF, $K\alpha$), metallic cobalt (Co, LIF, $K\alpha$), albite (Na, TAP, $K\alpha$), orthoclase (K, PET, $L\alpha$), sphalerite (Zn, LIF, $K\alpha$). Point analyses were performed directly on the carbon-coated surface of the sample on selected spots corresponding to different ROIs in order to probe both the fragments of the saprolite and the garnierite veins.

The mineral chemical compositions obtained by means of EMPA on the different samples are listed in **Table 1**, including the talc fraction (X_{talc}) of garnierites calculated according to Brindley and Hang (1973). The accepted totals are low because of the heterogeneity and the porosity of the samples falling below the spatial resolution of the EMPA, and the presence of structural and adsorbed water (Villanova-de-Benavent et al., 2016). The analyzed data points of the five samples were plotted in the ternary (Mg+Fe):Ni:Si diagram showing the composition of the garnierite types and the saprolite fragments (**Fig. 2**). This diagram also displays the compositional fields of the five garnierite types in Falcondo established by Villanova-de-Benavent et al. (2014) to demonstrate the representativeness of the samples selected.

2.4. Synchrotron experiments

In the present work the synchrotron experiments were performed on beamline 10.3.2 at the Advanced Light Source (Marcus et al., 2004). This is a hard X-ray microprobe on a bending magnet, delivering a monochromatic beam with a spot size ranging from about 1 to 15 μm . It is a dedicated beamline for environmental sciences with a 2-bounce Si(111), water cooled monochromator that covers the energy range from 2.45 keV to about 17 keV, and a 7 element Canberra Ge detector. The experiments consisted of three steps as in Mosselmans et al., (2008, 2009) and Roqué-Rosell et al., (2010). The first step involved identifying a suitable area of the sample by screening it and looking at the X-ray fluorescence counts from the multi-channel analyzer (MCA). Secondly X-ray fluorescence (μXRF) distribution maps of several elements were obtained for the chosen ROI. The final step involved collecting X-ray absorption spectroscopy (μXAS) spectra from one or more spots of interest identified by the μXRF mapping.

2.4.1. μXRF

The μXRF elemental maps were obtained by taking into account the intensity of the fluorescence lines corresponding to Cr K α at 5.415 keV, Fe K α at 6.405 keV and Ni K α at 7.48 keV, when rastering 4x4 mm cross sections on selected ROIs at 2° to the beam. This fluorescence geometry was used to minimize overabsorption in the subsequent experiments below. The incident X-ray beam size was $\sim 5 \times 5 \mu\text{m}$ (v. \times h.) and the step size of 5 μm (which fits within the mineral aggregate size range from 10 to 500 μm) using an incident excitation energy of 10 keV. The dwell times used were of 30–50 ms per point to prevent saturating the detector (270×10^3 cts/s). The obtained distribution of these elements is shown in the tricolor map in **Fig. 3**.

To assess the relationships between Fe and Ni from the saprolite fragments and the garnierite veins the scatter plots corresponding to Ni K α and Fe K α fluorescence intensities from each pixel on the ROIs μXRF maps were obtained in **Fig. 4**. Data points in the scatter plot aligned with a positive slope indicated that both Ni K α and Fe K α intensities are present and are cross-correlated. When the slope is negative Ni K α and Fe K α are excluding each other and are not correlated. When more than one cloud of data appear it means that the plotted elements are present in two or more non-related phases.

In addition, a chemical-state map for Fe was acquired to plot the distribution of the different Fe-bearing phases present in the samples. The Fe chemical-state map relies on the fact that the edge position for the Fe-K XANES shifts as a function of the Fe valence state. Thus, illuminating the sample at different energies allowed plotting the corresponding variations of Fe K α related to the different Fe chemical species. These maps, with fluorescence signals measured at different energies, can be stacked and combined into a multi energy map that is capable of providing a rough Fe K-edge XANES spectrum for each measured pixel. In the present paper, in order to obtain the Fe⁺² and the Fe⁺³ distributions, a set μXRF maps were obtained at energies of 7.1, 7.11, 7.113, 7.125, 7.133, 7.35 and 10 keV. This allowed mapping at an energy just below, mapping at a range of energies just after and mapping at an energy far above the Fe K-edge.

The multi energy maps from each ROI in each sample were subsequently analyzed with weighted sums of the representative species found on the same samples. These representative Fe K-edge XANES spectra were used as single compounds and were fitted to every μXRF pixel across the different energies. This procedure, explained in detail in Sutton et al. (1995), allowed us to plot the distribution of the most relevant Fe bearing mineral phases with a $\sim 5 \mu\text{m}$ spatial resolution. The XY display and chemical-state map software for μXRF acquisition and analysis were used to obtain the

elemental and chemical-state maps respectively. These scripts are freely distributed and available at the ALS website <https://sites.google.com/a/lbl.gov/microxas-lbl-gov/software>.

2.4.2. μ XAS

In order to identify and quantify the Fe-bearing minerals in the samples, a range of Fe K-edge μ XANES were performed on representative selected spots in fluorescence geometry. A metal Fe foil was measured in transmission mode for calibration prior to the experiments. Every measurement was taken by scanning the monochromator about 300 eV above the Fe K-edge (7.112 keV). To optimize the signal to noise ratio, about 40 Fe-K XANES spectra were acquired at each point in Quick XAS (QXAS) scanning mode. In QXAS mode data is collected by scanning the monochromator in a continuous motion and taking the fluorescence data on the fly, as opposed to the step and-repeat mode. This mode allows one to acquire scans in as little as 10 seconds. The resulting spectra have been fitted by means of principal components analysis (PCA) using the PCA package that can be found at <https://sites.google.com/a/lbl.gov/microxas-lbl-gov/software>. This software implements the PCA as described by Ressler et al. (2000). It analyzes a set of spectra to see if each acquired measurement can be represented as linear combinations of a smaller number of component spectra. In the present study, a range of Fe-bearing mineral standards acquired at the ALS beamline 10.3.2 have been used to fit the measured Fe K-edge μ XANES.

The local environment of Ni within the samples was determined by means of Ni K-edge μ EXAFS following the same fluorescence geometry. A Ni metal foil was measured for calibration prior to the experiments. Each measurement was taken by scanning the monochromator about 700 eV above the Ni K-edge (8.333 keV). To optimize the signal to noise ratio as many as 500 Ni-K EXAFS spectra were acquired at each point in order to achieve sufficient data quality in QXAS mode. The EXAFS fittings were performed using the Athena package (Ravel and Newville, 2005) and the refinement included only single scattering events, to account for the averaged distances and the coordination numbers of Ni within the phyllosilicates. The parameters chosen to be refined corresponded to the atomic potentials, the interatomic distance, the Debye–Waller factor, and the shell occupancy numbers. The length of the EXAFS signal is important to determine the number of parameters available to fit according to the relationship described by Galois et al. (1995). In the present EXAFS experiments for a data length Δk of 9.5 \AA^{-1} and a filtering window in real space of about 2.1 \AA , the number of independent parameters N_{ind} that can be refined is 12.

The Ni local environment was fitted taking into account the parameters and constraints of Ni within the original mineral phases constituting the saprolite fragments and the garnierite veins. The structural model used in the fittings are constructed as radial shells with defined distances and coordinations about the target atom, in this case Ni, the first shell is the oxygens, the second shell is the Mg or Ni and the third shell is the Si. According to Manceau et al. (1985, 1986) and Manceau and Calas (1985), the interatomic distances between Ni and the second shell in Ni-bearing phyllosilicates should be close to 3.06 \AA . In addition, special attention was given to the nature of the second coordination shell. In EXAFS the phase shift of the scattered photoelectrons depends on the chemical nature of the backscattering atom. This allowed us to distinguish between Ni and Mg second coordination shells in phyllosilicates if some constraints are applied on Ni-Ni and Ni-Mg distances during the EXAFS fitting. However, there were not enough N_{ind} parameters to model multiple Ni-Ni and Ni-Mg environments simultaneously on the same spectrum.

Thus, to model the partial substitution of Ni by Mg within the crystalline structure the N_{ind} impose some limitations in terms of the EXAFS fittings in that we were only able to use one Ni or one Mg second coordination shell for one structural Ni site. This was overcome by performing simultaneously a linear combination with k^3 -weighted $\chi(k)$ for second shells, one corresponding to Ni and another to Mg. This implied refining the Ni and Mg shells with the constraint that these two components must sum to a total of one second shell to account for the structural Ni local environment. By doing that the same degree of disorder was also defined in Ni and Mg atoms contained in the second shell by forcing them to share the same Debye-Waller factor. This additional last assumption kept the N_{ind} acceptable, while also allowing an assignment of the amount of Ni and Mg atoms comprising the second shell.

3. Results

3.1. Mineral textures

In **Fig. 1** two groups of samples can be seen, one corresponding to fragments of saprolite cemented by green and fine grained garnierite (**Fig. 1 a-d**), and one corresponding to massive green garnierite (**Fig. 1 e**). All samples exhibit different shades of green and textures as a function of the mineralogy and chemistry as described in Villanova-de-Benavent et al. (2014, 2016). Each selected ROI (red box) within each sample contains a representative selection of the mineral assemblages that correspond to the different garnierite types in Falcondo.

Under the OM the ROI from sample LC101A in **Fig. 1a** corresponds to saprolite fragments containing some altered chromian spinel grains, cemented by pale green Type I garnierite veins. The ROI from sample LC100B on **Fig. 1b** contains saprolite fragments cemented mostly by yellowish green Type II garnierite and turquoise Type IV garnierite, with euhedral quartz crystals filling the voids. The ROI from sample GAR2C on **Fig. 1c** consists of saprolite fragments coated by bright green Type III garnierite, which is intergrown with quartz crystals. The presence of euhedral quartz filling voids and coating garnierites indicates that these garnierites precipitated in open spaces from an aqueous solution. The ROI from sample GAR6C in **Fig. 1d** can be described as saprolite clasts surrounded by a turquoise-colored matrix of Type IV garnierite. Under the OM, this matrix consists of garnierite fragments cemented by a later garnierite precipitate with minor amounts of quartz. Sample FALC3 was identified as Type V and displays light green, undulated bundles of fibers accompanied only by tiny quartz veinlets with no traces of saprolite (**Fig. 1e**).

3.2. Chemical composition

The chemical composition of the secondary Ni-bearing serpentine from the saprolite fragments in samples LC101A, LC100B, GAR2C, GAR6C and FALC3 sit on the lizardite/chrysotile and spread over towards de falcondoite compositional domain (**Fig. 2**). The chemical composition of Type I, II and III garnierite veins plot between the lizardite/chrysotile-népouite/pecoraite and kerolite-pimelite series (**Fig. 2**). Type I garnierite has the lowest Ni content (1.19—8.92 wt.% NiO) and remarkable Fe (2.65—8.91 wt.% Fe_2O_3) (**Table 1, Fig. 2**). Type II garnierite has a higher Ni content (21.64—24.5 wt.% NiO) and much lower Fe content (0.46—0.66 wt.% Fe_2O_3) than Type I (**Table 1, Fig. 2**). Type III garnierite is closer to the pimelite end member (29—41 wt.% NiO) and no significant amounts of Fe (**Table 1, Fig. 2**). The type IV garnierite in sample GAR6C plots in a range of compositions between the kerolite-pimelite end members with 24.2—31.8 wt.% NiO and no detectable Fe (**Table 1, Fig. 2**). Finally, Type V garnierite in sample FALC3 plots in the sepiolite-falcondoite series.

Like Type IV, Type V garnierite displays a wide range of Ni contents (12.3—26.8 wt.% NiO) with no significant amounts of Fe (**Table 1, Fig. 2**). The overall analyzed spots show a trend that is characteristic of the five Types of garnierites in the Falcondo Ni-laterite deposit described by Villanova-de-Benavent et al., (2014, 2016).

3.3. Elemental Fe, Cr and Ni distribution obtained by means of μ XRF

The elemental maps obtained on the ROIs in samples LC101A, LC100B and GAR2C display variations in the elemental distribution of Ni, Cr and Fe that highlight the chemical and textural relationships between the saprolite fragments and the garnierite veins (**Table 1, Fig. 2**). In addition, some differences were observed between the garnierites in GAR6C and FALC3 ROIs on Ni distribution providing important hints on garnierite composition and texture (**Table 1, Fig. 3**).

The elemental distribution of Ni, Cr and Fe within the LC101A and LC100B ROIs show that Fe is associated with the saprolite fragments, Ni is localized mostly in the garnierite veins and Cr occurs within the saprolite fragments as altered chromian spinel. The obtained Ni:Fe scatter plot for LC101A in **Fig. 4(a, b)** displays five clouds of pixels. Two correspond to Fe $K\alpha$ fluorescence intensities not related to Ni $K\alpha$, which represent a combination of Ni-poor primary serpentine and Fe oxyhydroxides and the altered chromian spinel grains. A third group corresponds to pixel fluorescence intensities of Ni $K\alpha$ not related to Fe $K\alpha$, which can be interpreted as the presence of tiny Type IV garnierite veinlets crosscutting the saprolite fragment. In the fourth group Ni and Fe are positively correlated, and represents the Ni-bearing secondary serpentine constituting the bulk of the saprolite fragment. Finally, in the last group Ni and Fe are anti-correlated, and corresponds to the Fe-bearing Type I garnierite.

The mapping on LC100B on **Fig.3** displays some voids corresponding to the secondary precipitated quartz. The obtained Ni:Fe scatter plot from LC100B in **Fig. 4(a, c)** displays three groups of pixels. One group, where Fe shows a positive correlation with Ni, is interpreted as the Ni-bearing secondary serpentine from the saprolite. A second group, where Ni is not related to Fe and represents the type II and IV garnierites observed in the ROI. Finally, the inset graph **Fig. 4(c)** shows a small third group where Ni intensity is anti-correlated to Fe intensity (~30-80 cts/s) but is much less significant than in LC101A. This third cloud corresponds to possible remains of Type I garnierite.

The elemental distribution of Fe, Cr and Ni within the GAR2C ROI on **Fig. 3** shows a heavily weathered saprolite that contains most of the Fe. The saprolite fragments are enclosed within a Ni rim and contain some tiny Cr spots corresponding to altered chromian spinel. The elemental map displays a complete separation between Fe-bearing and Ni-bearing phases. This is also confirmed by the Ni:Fe scatter plot **Fig.4 (a, d)** where only two clouds of pixels are present. The first cloud represents a combination of Fe oxyhydroxides and minor amounts of serpentine, whereas the second cloud corresponds to the Type III garnierite.

The elemental distribution of Ni, Cr and Fe within the saprolite free GAR6C and FALC3 ROIs are shown in **Fig. 3**. Both samples show a high content of Ni across the ROI with no detectable amounts of Fe or Cr. However some variations in Ni concentrations can be seen in the elemental maps. In GAR6C, these variations allowed garnierite fragments (with lower Ni content, in dimmer green color) to be distinguished from garnierite matrix (with higher Ni content, in brighter green color) in the garnierite breccia. In contrast, the mapping on FALC3 shows a Ni distribution

matching the distinctive fibrous texture of the sepiolite-falcondoite series. In this case Ni is more concentrated in the edges of some fibrous aggregates.

3.4. Fe K-edge XANES for the identification of Fe-bearing phases and Fe speciation

The Fe-bearing mineral phases were identified and quantified in the ROIs for samples LC101A, LC100B and GAR2C (**Fig. 3**). The standards used correspond to the mineral phases previously identified in the saprolite horizon and correspond to a varying mixture of magnetite, serpentine, maghemite and goethite (Villanova-de-Benavent et al., 2014). The observed mineral compositions of the saprolite fragments show changes which are in agreement with the weathering processes affecting the saprolite during garnierite formation.

The Fe chemical-state map for LC101A plots the distribution of Fe⁺² and Fe⁺³ (**Fig. 3**). The map demonstrates that Fe⁺² is confined to veinlets within the saprolite and that Fe⁺³ constitutes the rest of the saprolite fragments and the surrounding Type I garnierite. In addition, the texture displayed in the chemical-state maps in **Fig. 3** indicates that the Fe⁺² rich veinlets probably correspond to remnants of Ni-poor primary serpentines of hydrothermal origin and traces of magnetite as in Andréani et al. (2013). According to the results in **Table 2**, the Fe⁺² on LC101A_1 is associated with Ni-poor, primary serpentine and was fitted with 48 % serpentine, 33 % magnetite and 20 % forsterite (**Fig. 5a**) and Fe⁺³ on LC101A_2 corresponds to the bulk saprolite with 66 % serpentine, 24 % maghemite and 10 % magnetite, (**Fig. 5b**). The Fe-K edge XANES fitting on LC101A_3 on Type I garnierite confirms that Fe is more oxidized and was fitted with 77 % serpentine and 22 % maghemite (**Fig. 5c**). Thus the chemical-state map shows the distribution of primary serpentine, magnetite and forsterite containing most of the Fe⁺², and the secondary serpentine, maghemite and goethite containing most of the Fe⁺³.

The distribution of Fe⁺² and Fe⁺³ in LC100B shows ferrous Fe fraction confined to veins within the saprolite and that ferric Fe fraction constitutes the rest of the saprolite fragment (**Fig. 3**). As in sample LC101A, the texture displayed in the chemical-state map indicates that the Fe⁺² rich veinlet probably corresponds to Ni-poor primary serpentines. Two Fe K-edge XANES were acquired to identify the main phases constituting the Fe⁺² rich vein (LC100B_1) and the bulk of the saprolite fragment with a high content of Fe⁺³ (LC100B_2). According to the data in **Table 2** the ferrous Fe in LC100B_1 was fitted with 59 % serpentine, 18 % maghemite, 14 % magnetite, and 10 % goethite (**Fig. 5c**) and the more oxidized Fe on LC100B_2 was fitted with 36 % serpentine, 35 % maghemite and 30 % goethite (**Fig. 5d**). Thus the chemical-state map shows the distribution of weathered serpentine and magnetite still containing some of the Fe⁺², and important amounts of goethite mixed with serpentine and maghemite containing most of the Fe⁺³.

The distribution of Fe⁺³ rich phases in GAR2C (**Fig. 3**) shows that the Fe⁺³ constitutes the whole of the saprolite portion and no unweathered primary hydrothermal serpentine with reduced Fe was detected. Fe K-edge μ XANES data (**Table 2**) acquired on one the GAR2C_2 representative point of the protolith fragment (**Fig. 5e**) showed that the Fe was present mostly in oxidized form with a composition of serpentine 31%, maghemite 51% and goethite 18%. This data confirms that in GAR2C significant amounts of goethite started to develop suggesting an advanced weathering stage of the saprolite fragments.

3.5. Ni crystallochemistry studied by means of Ni K-edge EXAFS

To study the Ni local environment in saprolite, Ni K-edge μ EXAFS spectra in the k range 2.5–12 (\AA^{-1}) were acquired at representative points on LC101A, LC100B and GAR2C samples (Fig. 6). The analyzed points correspond to saprolite fragments and garnierite veins with significant Ni content with the aim to elucidate differences in the local environment from lizardite-chrysotile within the saprolite and lizardite/chrysotile-népouite/pecoraite and kerolite-pimelite mixtures constituting the garnierites.

For LC101A three Ni K-edge μ EXAFS were acquired corresponding to the Ni-poor primary serpentine veins within the saprolite fragments labeled LC101A_1, the second point corresponds to Ni-bearing secondary serpentine on the saprolite fragment labeled LC101A_2 and the third point corresponds to the Type I garnierite surrounding the saprolite fragments, labeled LC101A_3 (Fig. 3 and 6). Qualitatively the EXAFS from LC101A_1 and LC101A_2 spots show significant differences when compared to the EXAFS from spot LC101A_3. The EXAFS from the saprolite fragments LC101A_1 and LC101A_2 have damped oscillations at $k \sim 8 \text{\AA}^{-1}$ and $k \sim 11 \text{\AA}^{-1}$ when compared to LC101A_3 from garnierite Type I. These differences are clearly seen as well by the corresponding $\text{FT}(\chi(k))$ second shell peaks between ~ 2 and 3.5\AA . The second shell peak is clearly enhanced in LC101A_3 in contrast to that in LC101A_1 and LC101A_2 which is strongly indicative of different Ni local environments in garnierite and saprolite.

The $\text{FT}(\chi(k))$ prominent second peak at 2.8–2.9 \AA on LC101A_3 in Fig. 6 suggests a second atom shell of higher atomic number when compared to LC101A_1 and LC101A_2 (Dublet et al., 2012). The EXAFS fitting values in Table 3 demonstrates that the second shell peak for LC101A_3 in the garnierite matrix can be fitted with 5.2 Ni at 3.04 \AA and 3.8 Si at 3.17 \AA . The Ni-Ni distances of approximately 3.06 \AA are consistent with edge-sharing NiO_6 and the Ni-Si distance of approximately 3.3 \AA is consistent with edge-sharing between SiO_4 tetrahedra and NiO_6 octahedra in lizardite-népouite and kerolite-pimelite mineral series (Manceau et al., 1985, Manceau and Calas, 1985, 1986). The EXAFS from LC101A_1 on Fig. 6 shows that $\text{FT}(\chi(k))$ peak can be fitted with two shells one with 4.6 Mg at 3.0 \AA and a second with 3.1 Si at 3.3 \AA as shown on Table 3. In this site the Ni-Mg distances and the Ni-Si distances are consistent with the Ni local environment within Ni-poor serpentine from New Caledonia (Dublet et al., 2012). For LC101A_2, however, the second shell peaks have an even better fit not with a site comprising Ni-Mg and Ni-Si shells, but with a Ni site that has a Ni-Ni shell partially substituted by Mg. The EXAFS from LC101A_2 (Fig. 6) shows that the $\text{FT}(\chi(k))$ peak can be fitted with a 2.9 Ni shell partially substituted by 3.1 Mg at 3.06 \AA as shown on Table 3. In this site the Ni-Ni and Ni-Mg distances are close to 3.06 \AA and the Ni-Si distances are close to 3.3 \AA , which are again consistent with the Ni local environment within Ni-bearing serpentine from the saprolite studied New Caledonia (Dublet et al., 2012). It should be noticed that the $\text{FT}(\chi(k))$ from LC101A and LC101A_2 have a prominent shoulder at the low- R side of the first peak which is associated to the noise at the high end of the EXAFS signal at $k > 10 \text{\AA}^{-1}$.

For LC100B the Ni K-edge μ EXAFS were acquired for two representative points. The first on the saprolite fragment corresponds to the remains Ni-bearing secondary serpentine labeled LC100B_1 and the second on the garnierite vein corresponds to the Type II garnierite labeled LC100B_2 (Fig. 3 and 6). As in sample LC101A the spectra from sample LC100B show significant differences in the Ni local environment from saprolite to garnierite that are visible in the corresponding $\text{FT}(\chi(k))$ second shell peaks between ~ 2 and 3.5\AA and that have been assessed with the analysis of the Ni K-edge μ EXAFS spectra. The prominent second peak at 2.8–2.9 \AA on LC100B_2 suggests a second atom shell of higher atomic number in Type II garnierite than that for the second atom shell on

LC100B_1 in the Ni-bearing secondary serpentine. The EXAFS fitting values on **Table 3** show that the second shell peak for LC100B_2 can be fitted with a shell combination of 5.22 Ni at 3.08 Å and 4.24 Si at 3.21 Å. The Ni-Ni distances are close to 3.06 Å and are consistent with those kerolite-pimelite and lizardite-népoite mineral series (Manceau et al., 1985, Manceau and Calas, 1985, 1986). On LC100B_1 the second shell peak has a better fit with a Ni site with a second Ni-Ni shell partially substituted by Mg at 3.08 Å with 5.7 Ni and 0.3 Mg and 3.9 Si at 3.17 Å. In this site the Ni-Ni and Ni-Mg distances are close to 3.06 Å which are consistent with the Ni-Mg mixed local environment within Ni-bearing serpentines from New Caledonia (Dublet et al. 2012).

For GAR2C only a single Ni K-edge μ EXAFS was acquired on the Type III garnierite coating labeled GAR2C_1 since no significant amounts of Ni were detected in the saprolite fragments (**Fig. 3** and **6**). Qualitatively the GAR2C_1 spectra shows similar $FT(\chi(k))$ features to the LC101A_3 and LC100B_2 with a significant peak between ~ 2 and 3.50 Å which is clearly characteristic of the Ni-Ni clustering within the mixture of lizardite/chrysotile-népoite/pecoraite mineral series and kerolite-pimelite mineral series that constitute the previous garnierites. The prominent $FT(\chi(k))$ second shell peak at 2.8–2.9 Å on GAR2C_1 can be fit with a combination of 3.72 Ni at 3.08 Å and 2.04 Si at 3.24 Å as shown on **Table 3**. The Ni-Ni distances are close to 3.06 Å and are consistent with edge-sharing NiO_6 and the Ni-Si distance is close to 3.3 Å and is consistent with edge-sharing between SiO_4 tetrahedra and NiO_6 octahedra in the lizardite-népoite and kerolite-pimelite series (Manceau et al., 1985, Manceau and Calas, 1985, 1986). However, the coordination of Ni-Ni is slightly defective suggesting a highly disordered local environment linked to the recrystallization processes that replace serpentines by talc in garnierites, as seen on Villanova-de-Benavent et al. (2016).

To study the Ni local environment in saprolite free garnierite Ni K-edge μ EXAFS were acquired on representative points in GAR6C and FALC3 (**Fig. 7** and **8**). The analyzed points correspond to characteristic heterogeneities in Ni content with the aim to elucidate if these variations correspond to distinctive Ni local environments in the kerolite-pimelite and sepiolite-falcondoite mineral series. On GAR6C four Ni K-edge EXAFS were acquired corresponding to the garnierite Type IV fragments with lower Ni content labeled GAR6C_1, GAR6C_3, GAR6C_4 and GAR6C_5 and two corresponding to the garnierite Type IV veins with higher Ni content labeled GAR6C_2 and GAR6C_6. Their $FT(\chi(k))$ show the distinctive second shell peaks at 2.8–2.9 Å with no significant qualitative differences across the selected points (**Fig. 7**). Their second shell peak is as prominent as in LC101A_3, LC100B_2 and GAR2C_1 indicative of GAR6C sharing the same similarities in terms of Ni local environment as in Type I, II and III garnierites (**Fig. 6** and **7**).

Most of the analyzed spots on GAR6C show $FT(\chi(k))$ prominent, second shell peaks that were fitted with a combination of ~ 5 Ni at ~ 3.06 Å and ~ 3 Si at ~ 3.3 Å except for GAR6C_6 (**Fig. 7** and **Table 4**). The later has a second shell depleted in Ni and the third shell enriched in Si, that could be explained by a higher degree of local disorder linked to the ongoing recrystallization process taking place in garnierites (Villanova-de-Benavent et al. , 2016) . Thus, in Type IV garnierites the distances obtained are consistent with edge-sharing NiO_6 and with edge-sharing between SiO_4 tetrahedra and NiO_6 octahedra in the kerolite-pimelite series determined by Manceau et al. (1985) and Manceau and Calas (1985, 1986) but with lower coordination numbers. The lower coordination for Ni–Ni and Ni–Si shells are thought to be related to the highly disordered nature of Type IV garnierite. According to Villanova-de-Benavent et al. (2016) Type IV garnierite underwent a dissolution-precipitation process where lizardite/chrysotile-népoite/pecoraite were completely replaced by kerolite-pimelite with a very low crystallinity. The modelling of the EXAFS

data as shown in **Table 4** suggests that the Ni local environment is fairly similar between the fragments and the coatings in the GAR6C breccia (**Fig. 7** and **Table 4**).

On FALC3 four Ni K-edge EXAFS were acquired corresponding to the garnierite Type V with low Ni content labeled FALC3_2, FALC3_3, FALC3_5 and FALC3_6 and two corresponding to the garnierite Type V with high Ni content labeled FALC3_1 and FALC3_4 (**Fig. 8**). Their $FT(\chi(k))$ show the distinctive second shell peak at 2.8–2.9 Å with no significant qualitative differences across the analyzed points. However its $FT(\chi(k))$ show some specificities when compared to the previous garnierites with a second shell peak less prominent than the garnierites in LC101A_3, LC100B_2 and GAR2C_1 and GAR6C_1-6 but more prominent than in the saprolite in L101A_1-2 and LC100B_1. Thus second $FT(\chi(k))$ peak suggests some subtle differences in the Ni local environment within the sepiolite-falcondite series when compared to the local environment within the mixture of lizardite/chrysotile-népouite/pecoraite series and kerolite-pimelite mineral series constituting the previous garnierites (**Fig. 6, 7** and **8**).

The height of the $FT(\chi(k))$ second shell peak at 2.8–2.9 Å on FALC3 suggests that the second shell atoms are still of Ni. The obtained EXAFS fitting values listed in **Table 5** demonstrate that this second peak can be fitted with a combination of Ni and Si with coordination numbers close to ~3 and ~4 and with the Ni-Ni distances close to 3.06 Å and the Ni-Si distance close to 3.3 Å. As in the previous samples for Type V garnierite the distances obtained were consistent with edge-sharing NiO_6 and with edge-sharing between SiO_4 tetrahedra and NiO_6 octahedra determined by Manceau et al. (1985) and Manceau and Calas (1985, 1986). However, the low coordination values for the second coordination shell suggest that the second shell is consistently depleted in Ni when compared to the previous Types I, II, III and IV garnierites.

4. Discussion

4.1. The precipitation of garnierites in the Falcondo Ni-laterite deposit

The garnierite veins display a diversity of Ni content and textures corresponding to the different precipitation and dissolution episodes that took place during their development. Coupling the OM and EMPA measurements provided an opportunity to study the garnierites' texture and chemical composition during the evolution of the Ni-laterites. Thus the successive enrichment of Ni observed through Type I, II and III garnierites can be explained by the increase of X_{talc} in the garnierite mixture, as reported by Soler et al. (2008) and Villanova-de-Benavent et al. (2014, 2016). However Ni is highly variable in garnierite Types IV and V, which in addition to the textural features (garnierite breccias in Type IV and variable Ni contents across the bundles of fibres in type V; **Fig. 2** and **3**) is explained by recurrent changes in the Ni content from the Ni-saturated aqueous solution percolating from the upper horizons (Villanova-de-Benavent et al., 2014). It should be noticed that while garnierites are neoformed secondary phases precipitated in open spaces, secondary Ni-bearing serpentines from the saprolite are suggested to be formed by Ni-Mg substitution in the octahedral sites of the serpentine structure (e.g. Freyssinet et al., 2005).

The increase of the SiO_2 content from Type I to Type V garnierites is in agreement with the dissolution of the primary ultramafic rock leading to the progressive silicification within the laterites (**Fig.1** and **2**). According to Trescases (1975), Golightly (1981), Freyssinet et al. (2005) and Soler et al. (2008) there is an increase in the silica activity during the formation of garnierites linked to the release of Mg and Ni in phyllosilicates and the development of silica rich surfaces.

During this process, the dissolving events at slightly alkaline pH (>8-9) at the base of the lateritic profile mobilize the accumulated silica increasing the silica activity in the aqueous solutions. These combined and repeated cycles of dissolution and precipitation in Falcondo explain the formation of phases progressively enriched in silica: from Ni-bearing serpentine to kerolite-pimelite and finally sepiolite-falcondoite in garnierite as described in Galí et al. (2012).

4.2. Ferrous versus ferric iron in the saprolite horizon

The chemical state maps allowed distinguishing the Ni-bearing secondary serpentine and Fe-bearing Type I garnierite from the Ni-poor primary serpentine (of hydrothermal origin) by the oxidation state of iron. The chemical distribution of Fe rich phases displays a texture with the most reduced forms of Fe associated to the primary Ni-poor serpentines (as reported by Andréani et al., 2013) whilst the more oxidized Fe is found associated with the secondary Ni-bearing serpentines within the bulk of the saprolite and Type I garnierite (**Fig. 3** and **4**). The primary ferromagnesian anhydrous silicates (mostly olivine and pyroxene) of the serpentinized peridotite protolith are likely to be weathered when the ophiolite complex is exposed to the intense rainfall and temperatures of tropical latitudes. However, the primary Ni-poor serpentine veins formed prior to the exhumation, may remain more stable (e.g. Golightly, 1981; 2010) and have a small amount of Fe in the form of Fe²⁺. During the formation of the Ni-laterite profile the primary minerals are altered to the Ni-bearing serpentine that constitutes the bulk of the saprolite horizon, in which Fe is mostly in the Fe³⁺ form (**Fig 3** and **Fig. 5**). In the case of Type I garnierite the iron is thought to be residual (Villanova-de-Benavent et al., 2014, 2016).

4.3. The Ni local environment in the saprolite horizon

The Ni crystallochemistry within the saprolite fragments showed differences related to weathering processes and associated to garnierite development. The FT($\chi(k)$) second peak at 2.8–2.9 Å from Ni K-edge μ EXAFS shows a steady increase in height linked to changes in the local Ni environment that occur through weathering affecting the Ni-poor primary serpentines on LC101A_1 to Ni-bearing secondary serpentines on LC100B_1 and the development of the garnierite on LC101A_3 (**Fig. 9**). The FT($\chi(k)$) second peak from Ni-poor primary serpentines on LC101A_1 and the FT($\chi(k)$) second peak from the Ni-bearing secondary serpentines LC101A_2 share the same features with Ni as a homogeneous solid solution with Mg (**Fig. 9**). However the FT($\chi(k)$) second peak from LC100B_1 compared to LC101A_1 depicts a decrease of the amount of Mg in the second coordination shell which is balanced with an increase of the Ni (**Fig. 9**). The FT($\chi(k)$) second peak from Type I garnierite on LC101A_3 completes the trend observed for LC100B_1 with the Ni local sites completely surrounded by Ni (**Fig 9**).

The later stages of garnierite formation are observed on samples GAR2C, GAR6C and FALC3. The corresponding FT($\chi(k)$) second shell peaks at 2.8–2.9 Å from the measured Ni K-edge μ EXAFS are well developed but with some minor differences between the kerolite-pimelite garnierite on GAR2C and GAR6C (**Fig.6, 7, 8**) when compared to the sepiolite-falcondoite garnierite on sample FALC3 (**Fig. 9**). Since the local environment of Ni in garnierites is only surrounded by a Ni second shell, the differences are thought to be related to the intrinsic crystal structure of the secondary phyllosilicates constituting the garnierites. Thus the differences seen in the FT($\chi(k)$) from Type V garnierite when compared to Type II, III and IV garnierites are thought to be related to Ni depleted second shells, which should be intrinsic of the structure of sepiolite.

The small decrease of the $FT(\chi(k))$ second peak in FALC3 is related to important discontinuities associated with the Ni octahedral site configuration within the sepiolite structure. The channels present in the sepiolite structure along the c axis truncate the horizontal layers of NiO_6 octahedra lowering the overall local Ni coordination in Ni-bearing sepiolite (Post et al., 2007). According to its symmetry the sepiolite structure has 4 Ni atoms in Wyckoff positions: Two Ni positions coordinated with another 6 second shell atoms, one Ni position coordinated with 5 second shell atoms and one last Ni position coordinated with 3 second shell atoms. This accounts for an average of 5 second shell atoms for each Ni position in sepiolite (Post et al., 2007). In the talc structure due to its lower symmetry, Ni atoms in Wyckoff positions are both coordinated to another 6 second shell atoms (Gruner, 1934). This should explain the differences observed in the $FT(\chi(k))$ second peak from Type V garnierite when compared to Types II, III, and IV and it is in agreement with the ideal second shell coordination for Ni being lower in sepiolite than in Talc (**Fig. 9**).

However, there are still some systematic differences from the expected ideal Ni-Ni second shell coordination number and the obtained values by means of Ni K-edge EXAFS. According to the synchrotron measurements the second Ni-Ni shell coordination number was systematically lower for garnierite samples when compared to the theoretical values for talc and sepiolite. These differences were not observed for the measured first Ni-O coordination shells, which remained close to the theory. The agreement with the experimental and theoretical coordination values for the Ni-O shells and the discrepancy with the experimental and theoretical coordination values for the Ni-Ni shells were indicative of a disordered material as demonstrated by Villanova-de-Benavent et al. (2014, 2016), and discounts other explanations affecting the $FT(\chi(k))$ peaks such as overabsorption.

5. Conclusions

By combining OM, EMPA analysis, μ XRF mapping, Fe K-edge μ XANES and Ni K-edge μ EXAFS with the information gathered from previous works, the following conclusions can be extracted on the garnierite development during the formation of the Falcondo Ni-laterite deposits.

The saprolite fragments consist mainly of Ni-Fe-enriched serpentines in which Fe is mostly in the ferric form (Fe^{3+}), and Ni is randomly distributed in the octahedral layer (homogeneous distribution) with small clustering. In addition, some remnants of the Ni-poor primary hydrothermal serpentine have been identified within the weathered protolith with a characteristic high fraction of Fe^{2+} and with a distinctive Ni local environment with Ni forming a homogenous solid solution with Mg.

All the garnierite types studied show similarities in the Ni distribution, regardless of the Ni content and the mineralogy. In all garnierites the Ni is found forming clusters (heterogeneous distribution). Within the serpentine and the kerolite-pimelite that constitute the Type I, II, III and IV garnierites Ni is surrounded exclusively by a second shell of Ni. This has been also the case on the sepiolite constituting the Type V garnierite, where Ni is found forming clusters with a depleted second shell which is consistent with the discontinuous octahedral layers within its structure.

The μ XAS results are consistent with the formation of the saprolite Ni-Fe-enriched serpentines from Ni-Mg substitution as a result of the interaction of the primary rock-forming minerals with a

Ni-enriched solution and of garnierites as precipitates from a Ni-Si-saturated aqueous solution at low temperatures.

ACKNOWLEDGEMENTS

This research has been financially supported by FEDER Funds, the Spanish projects CGL2009-10924 and CGL2012-36263 and Catalan project 2014-SGR-1661, and a PhD grant to Cristina Villanova-de-Benavent sponsored by the Ministerio de Educación (Spain). The beamtime provided by the Advanced Light Source was supported by the Director, Office of Science, Office of Basic Energy Sciences, U.S. Department of Energy under Contract DE-AC02-05CH11231. We would also like to thank the help and hospitality extended by the staff at Falcondo Glencore-Xstrata mine, especially by Francisco Longo. Professor J. F. Lewis is also gratefully acknowledged for his support during field work and his constructive comments.

REFERENCES

- Andreani M., Muñoz M., Marcaillou C., Delacour A. (2013). μ XANES study of iron redox state in serpentine during oceanic serpentinization. *Lithos*. 178, 70-83.
- Aiglsperger T., Proenza J.A., Zaccarini F., Lewis J.F., Garuti G., Labrador M., Longo F. (2015). Platinum group minerals (PGM) in the Falcondo Ni-laterite deposit, Loma Caribe peridotite (Dominican Republic). *Miner. Deposita* 50, 105-123.
- Aiglsperger T., Proenza J.A., Lewis J.F., Labrador M., Svojtka M., Rojas-Purón A., Longo F., Ďurišová J. (2016). Critical metals (REE, Sc, PGE) in Ni-laterites from Cuba and the Dominican Republic. *Ore Geol. Rev.* 73, 127-147
- Brindley G.W., Hang P.T. (1973). The nature of garnierite: I. Structure, chemical compositions and color characteristics. *Clay Clay Miner.* 21, 27-40.
- Brindley G.W. (1978). The structure and chemistry of hydrous nickel containing silicate and aluminate minerals. *Bull. BRGM* sec. II, 3 233-245.
- Butt C.R.M., Cluzel D. (2013). Nickel laterite ore deposits: weathered serpentinites. *Elements* 9, 123-128
- Decarreau A., Graby O., Petit S. (1992). The actual distribution of octahedral cations in 2:1 clay minerals: results from clay synthesis. *Appl. Clay Sci.* 7, 147-167.
- Dublet G., Juillot F., Morin G., Fritsch E., Fandeur D., Ona-Nguema G., Brown G.E.Jr. (2012). Ni speciation in a New Caledonian lateritic regolith: A quantitative X-ray absorption spectroscopy investigation. *Geochim. Cosmochim. Acta* 95, 119-133.
- Dzemua G. L., Gleeson S. A., Schofield P. F. (2013). Mineralogical characterization of the Nkamouna Co-Mn laterite ore, southeast Cameroon. *Miner. Deposita* 48, 155-171.

- Elias M. (2002). Nickel laterite deposits—Geological overview, resources and exploration. In: Cooke D, Pongratz J (Eds.), *Giant ore deposits—Characteristics, genesis, and exploration*. CODES Special Publication 4, University of Tasmania, Hobart, p. 205-220.
- Elias M., Donaldson M.J., Giorgetta N. (1981). Geology, mineralogy, and chemistry of lateritic nickel-cobalt deposits near Kalgoorlie, Western Australia. *Econ. Geol.* 76, 1775–1783.
- Fan R., Gerson A.R. (2011). Nickel geochemistry of a Philippine laterite examined by bulk and microprobe synchrotron analyses. *Geochim. Cosmochim. Acta* 75, 6400-6415.
- Freyssinet Ph., Butt C.R.M., Morris R.C. (2005). Ore-forming processes related to lateritic weathering. *Econ. Geol. 100th Anniversary Vol.*, 681-722.
- Fu W., Yang J.W., Yang M.L., Pang B.C., Liu X.J., Niu H.J., Huang X.R. (2014). Mineralogical and geochemical characteristics of a serpentinite-derived laterite profile from East Sulawesi, Indonesia: Implications for the lateritization process and Ni supergene enrichment in the tropical rainforest. *J. Asian Earth Sci.* 93, 74-88.
- Galí S., Soler J.M., Proenza J.A., Lewis J.F., Cama J., Tauler E. (2012). Ni-enrichment and stability of Al-free garnierite solid-solutions: a thermodynamic approach. *Clay. Clay Miner.* 60, 121-135.
- Galoisy L., Calas G., Brown Jr. G. E. (1995). Intracrystalline distribution of Ni in San Carlos olivine: An EXAFS study. *Am. Mineral.* 80, 1089-1092.
- Gleeson S.A., Butt C.R., Elias M. (2003). Nickel laterites: a review. *SEG Newsl.* 54, 11-18.
- Golightly J.P. (1979). Geology of Soroako nickeliferous laterite deposits. *Int. Laterite Symposium* 3, 38-55.
- Golightly J.P. (1981). Nickeliferous laterite deposits. *Econ. Geol. 75th Anniversary Vol.*, 710-735.
- Golightly J.P. (2010). Progress in understanding the evolution of nickel laterites. *Econ. Geol. Spec. Publ.* 15, 451-485.
- Gruner J.W. (1934). The crystal structure of talc and pyrophyllite. *Zeitschrift fur Kristallographie.* 88, 412-419.
- Kuck P.H. (2013). Nickel. *USGS Mineral Commodity Summaries*, 108-109.
- Lewis, J.F., Draper, G., Proenza, J.A., Espaillet, J., Jiménez, J. (2006). Ophiolite-related ultramafic rocks (serpentinites) in the Caribbean region: a review of their occurrence, composition, origin, emplacement and nickel laterite soils. *Geol. Acta* 4, 237–263.
- Manceau A., Calas G., Decarreau A. (1985). Nickel-bearing clay minerals: I. Optical spectroscopic study of nickel crystal chemistry. *Clay Miner.* 20, 367-387.
- Manceau A., Calas G. (1986). Nickel-bearing clay minerals: II. Intracrystalline distribution of Nickel: An X-ray absorption study. *Clay Miner.* 21, 341-360.

Manceau A., Calas G. (1985). Heterogeneous distribution of nickel in hydrous silicates from New Caledonia ore deposits. *Am. Mineral.* 70, 549-558.

Marcus M.A., MacDowell A.A., Celestre R., Manceau A., Miller T., Padmore H.A., Sbullett R.E. (2004). Beamline 10.3.2 at ALS: a hard X-ray microprobe for environmental and materials sciences. *J. Synchrotron Radiat.* 11, 239-247.

Mosselmans J.F.W., Quinn P.D., Roque-Rosell J., Atkinson K.D., Dent A.J., Cavill S.I., Hodson M.E., Kirk C.A., Schofield P.F. (2008). The first environmental science experiments on the new microfocus spectroscopy beamline at diamond. *Mineral. Mag.* 72, 197-200

Mosselmans J.F.W., Quinn P.D., Dent A.J., Cavill S.A., Diaz Moreno S., Peach A., Leicester P.J., Keylock S.J., Gregory S.R., Atkinson K.D., Roque Rosell J. (2009). I18 — the microfocus spectroscopy beamline at the Diamond light source. *J. Synchrotron Radiat.* 16, 818-824.

Mudd G.M. (2010). Global trends and environmental issues in nickel mining: sulfides versus laterites. *Ore Geol. Rev.* 38, 9-26.

Post J.E., Bish D.L., Heaney P.J. (2007). Synchrotron powder X-ray diffraction study of the structure and dehydration behavior of sepiolite. *Am. Mineral.* 92, 91-97.

Ravel B., Newville M., (2005). ATHENA, ARTEMIS, HEPHAESTUS: data analysis for X-ray absorption spectroscopy using IFEFFIT. *J. Synchrotron Radiat.* 12, 537-541.

Ressler T., Wong J., Roos J., Smith I.L. (2000). Quantitative Speciation of Mn-Bearing Particulates Emitted from Autos Burning (Methylcyclopentadienyl) manganese Tricarbonyl-Added Gasolines Using XANES Spectroscopy. *Environ. Sci. Technol.* 34, 950-958.

Roqué-Rosell J., Mosselmans J. F. W., Proenza J. A., Labrador M., Gali S., Atkinson K. D., Quinn P. D. (2010). Sorption of Ni by "lithiophorite-asbolane" intermediates in Moa Bay lateritic deposits, eastern Cuba. *Chem. Geol.* 275, 9-18.

Soler J.M., Cama J., Galí S., Meléndez W., Ramírez A., Estanga J. (2008). Composition and dissolution kinetics of garnierite from the Loma de Hierro Ni-laterite deposit, Venezuela. *Chem. Geol.* 249, 191-202.

Springer G. (1974). Compositional and structural variations in garnierites. *Can. Mineral.* 12, 381-388.

Sutton S.R., Bajt S., Delaney J., Schulze D., Tokunaga T. (1995). Synchrotron x-ray fluorescence microprobe: Quantification and mapping of mixed valence state samples using micro-XANES. *Rev. Sci. Instr.* 66, 1464-1467.

Tauler E., Proenza J.A., Galí S., Lewis J.F., Labrador M., García-Romero E., Suárez M., Longo F., Bloise G. (2009). Ni-sepiolite-falcondoite in garnierite mineralization from the Falcondo Ni-laterite deposit, Dominican Republic. *Clay Miner.* 44, 435-454.

Trescases J.J. (1975). L'évolution géochimique supergène des roches ultrabasiques en zone tropicale et la formation des gisements nickélifères de Nouvelle-Calédonie. Mémoires ORSTOM 78, p. 288.

Villanova-de-Benavent C., Proenza J.A., Galí S., García-Casco A., Tauler E., Lewis J.F., Longo F. (2014). Garnierites and garnierites: Textures, mineralogy and geochemistry of garnierites in the Falcondo Ni-laterite deposit, Dominican Republic. *Ore Geol. Rev.* 58, 91-109.

Villanova-de-Benavent C., Nieto F., Viti C., Proenza J.A., Galí S., Roqué-Rosell J. (2016). Ni-phyllosilicates (garnierites) from the Falcondo Ni-laterite deposit (Dominican Republic): mineralogy, nanotextures and formation mechanisms by HRTEM and AEM. *Am. Miner.* DOI: [10.2138/am-2015-5518](https://doi.org/10.2138/am-2015-5518)

Whitney D.L., Evans B.W. (2010). Abbreviations for names of rock-forming minerals. *Am. Miner.* 95, 185-187.

Figure 1. Images of the samples (left) and optical photomicrographs in plane polarized light of the regions of interest (ROI) selected to perform EMPA, μ XRF and μ XAS from samples **(a)** LC101A (saprolite and type I garnierite), **(b)** LC100B (saprolite and type II garnierite), **(c)** GAR2C (saprolite and type III), **(d)** GAR6 (type IV garnierite) and **(e)** FALC3 (type V garnierite). The brown fragments of the weathered saprolite are surrounded by the green garnierite veins.

Figure 2. Ternary plots showing the compositions of the analyzed garnierites compared to the five garnierite types described by (Villanova-de-Benavent et al., 2014). The compositions of the selected samples fall into the saprolite serpentine, and the garnierite Type I, II, III, IV and V fields. Abbreviations are after Whitney & Evans (2010), Tauler *et al.* (2009) and Villanova-de-Benavent *et al.* (2014), except Pec for pecoraite.

Figure 3. The μ XRF elemental maps (Fe K α in red, Ni K α in green and Cr K α in blue) and the chemical-state maps (in greyscale Fe⁺² and the Fe⁺³) showing ferrous veins within ferric saprolite fragments. The labelled points on the elemental map correspond to the spots where Ni-K EXAFS have been acquired and on the chemical-state maps correspond to the spots where Fe-K XANES have been acquired. The selected spots can be grouped in hydrothermal serpentine veins (LC101A_1 and LC100B_1), saprolite fragments (LC101A_2, LC100B_3 and GAR2C_2), Type I garnierite (LC100B_2), Type II garnierite (LC100B_2), Type III garnierite (GAR2C_1), Type IV garnierite (from GAR6_1 to GAR6_6) and Type V garnierite (from FALC3_1 to FALC3_6). The inset graph **(a)** shows the integrated XRF intensities at 10keV for samples LC101A, LC100B and GAR2C.

Figure 4. Ni K α vs Fe K α scatter plots for sample LC101A in blue, LC100B in green and GAR2C in red **(a)**. LC101A has a characteristic anticorrelation of Ni and Fe which corresponds to garnierite Type I surrounding the saprolite fragments **(b)**. The anticorrelation diminishes in LC100B4 and does correspond to the Ni-rich serpentine relicts present within the saprolite **(c)** and disappears in GAR2C **(d)**. The non-correlated Fe cts. corresponds to the saprolite fragments and the non-correlated Ni cts. to the garnierite matrix.

Figure 5. Fe K-edge μ XANES and the resulting fits with goethite (yellow), maghemite (red), serpentine (green) and forsterite (blue) **(a)** corresponds to LC101A_1 on the saprolite fragment **(b)** corresponds to LC101A_2 on the Ni-rich serpentine **(c)** corresponds to LC101A_3 on the Type I garnierite **(d)** corresponds to LC100B_1 on the serpentine vein and **(e)** corresponds to LC100B_2 on the saprolite fragment. **(f)** corresponds to GAR2C_2 on the saprolite fragment.

Figure 6. Ni K-edge μ EXAFS, the corresponding FT($\chi(k)$) and the resulting fits from samples LC101A, LC100B and GAR2C. Differences on the second shell peak height at 2.8-2.9 Å are clearly visible.

Figure 7. Ni K-edge μ EXAFS, the corresponding FT($\chi(k)$) and the resulting fits from sample GAR6C. No differences on the second shell peak height at 2.8-2.9 Å are visible despite of the differences of Ni content.

Figure 8. Ni K-edge μ EXAFS, the corresponding FT($\chi(k)$) and the resulting fits from sample FALC3. No major changes on the second shell peak height at 2.8-2.9 Å are visible.

Figure 9. Ni K-edge μ EXAFS from samples LC101A, LC100B, GAR2C and FALC3 showing the main differences on Ni local environment from primary Ni-poor serpentine (LC101A_1 and LC100B_1),

Fe-bearing serpentine from Type I garnierite (LC101A_3), from kerolite-pimelite from Type II and III garnierites (LC100B_2 and GAR2C_1) and sepiolite-falcondoite from Type V garnierites (FALC3_3).

ACCEPTED MANUSCRIPT

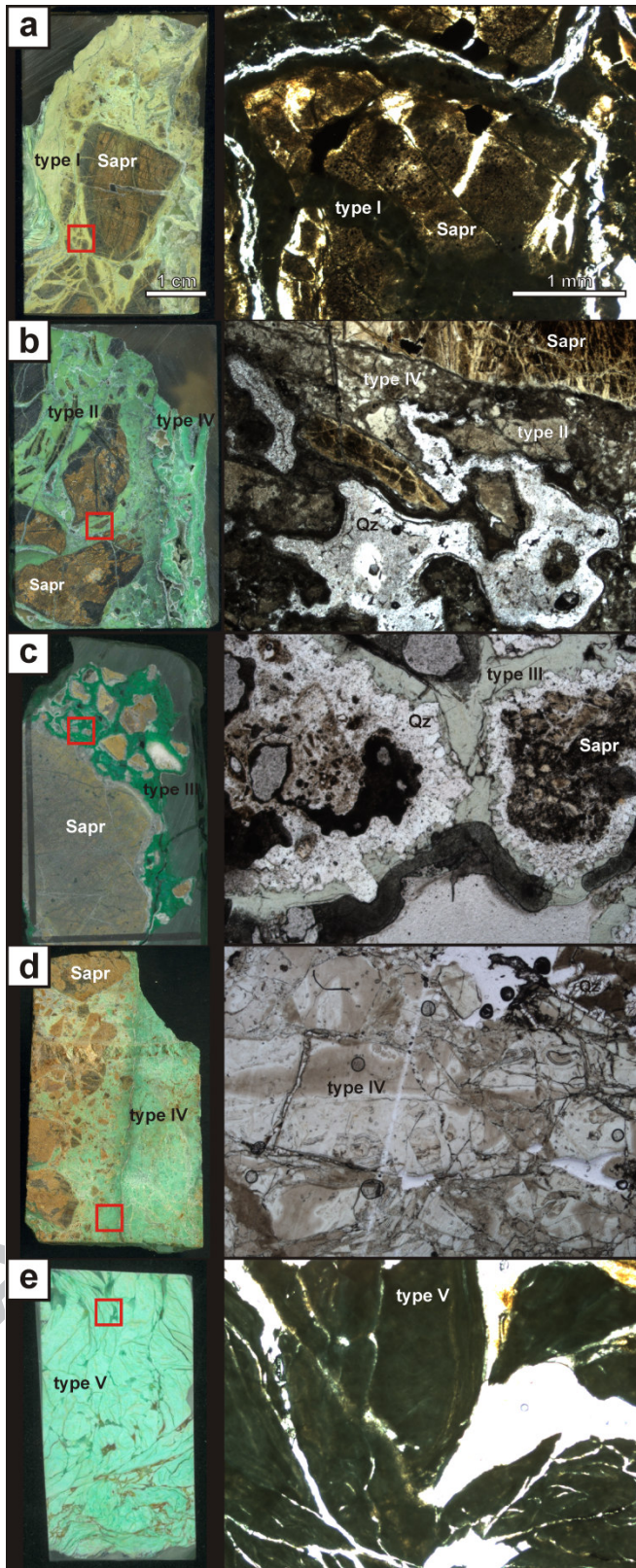


Figure 1

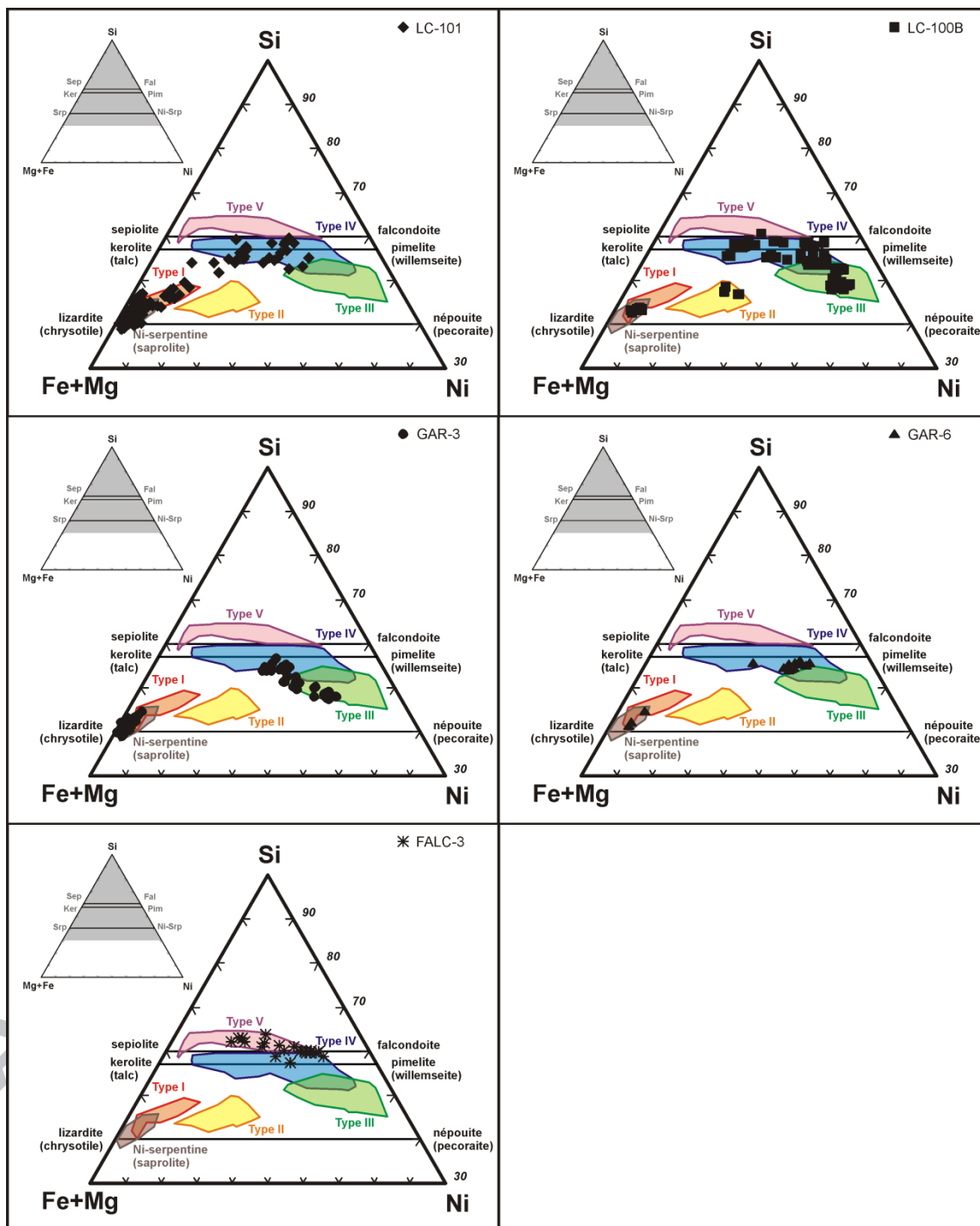


Figure 2.

ACCEPTED MANUSCRIPT

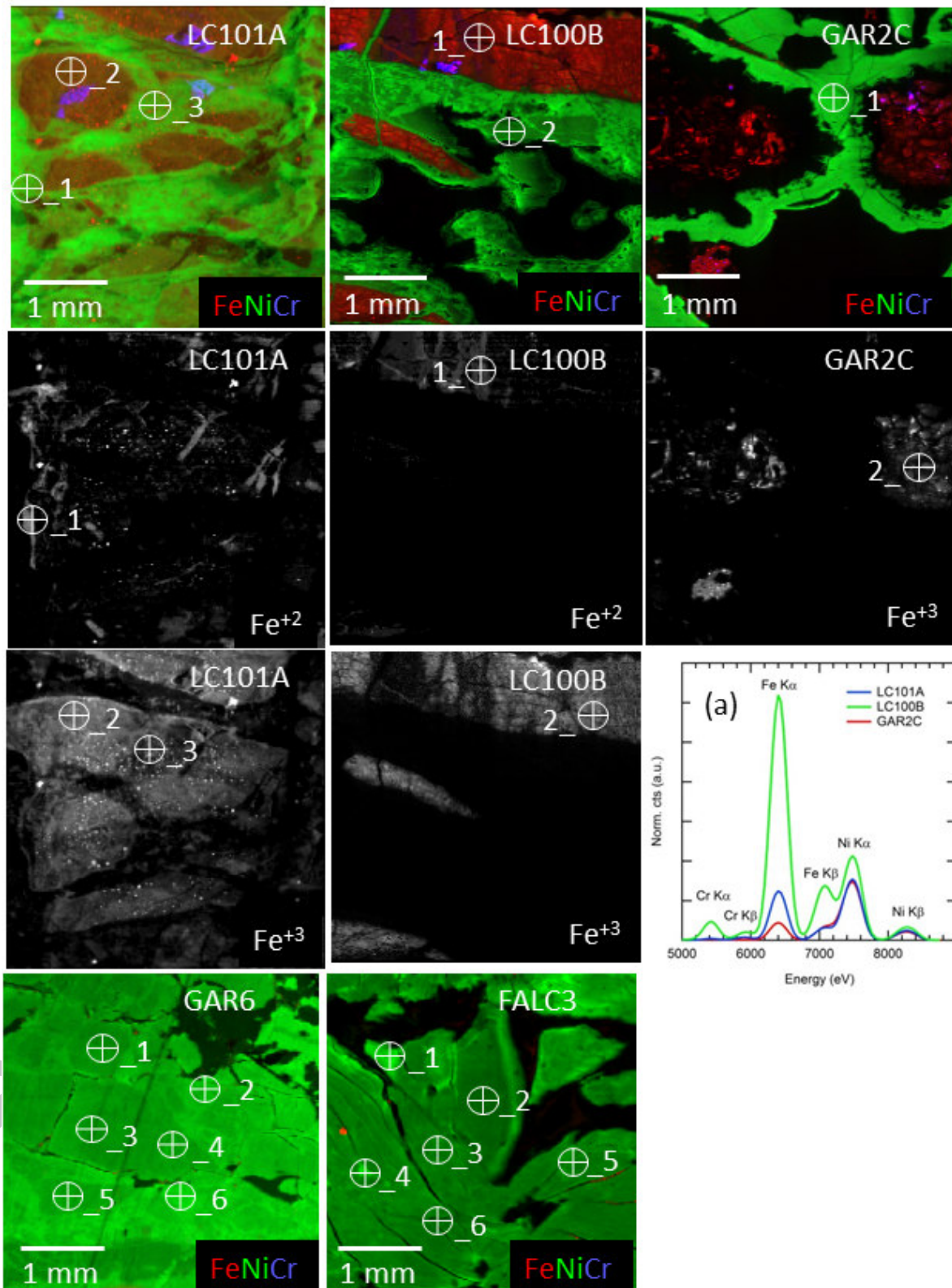


Figure 3.

ACCEPTED MANUSCRIPT

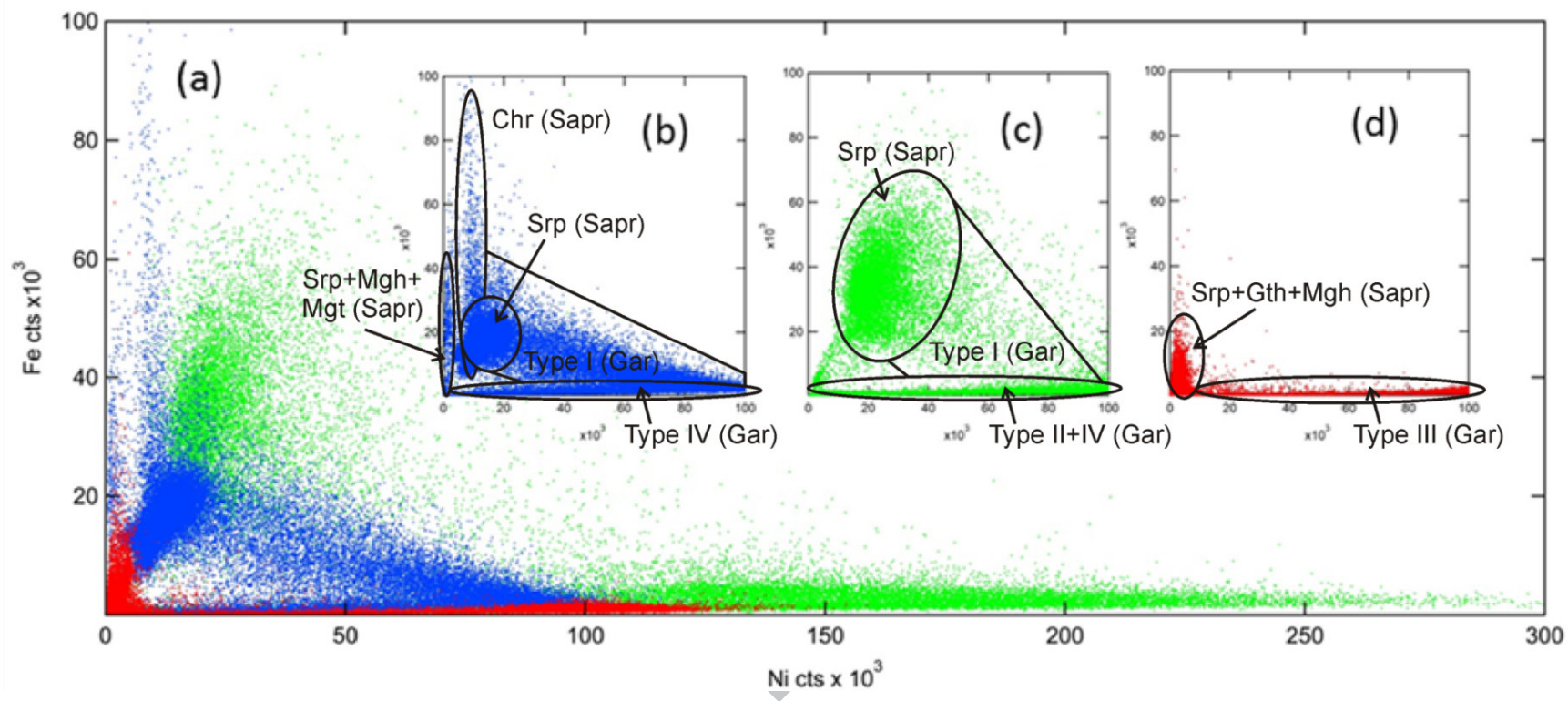


Figure 4.

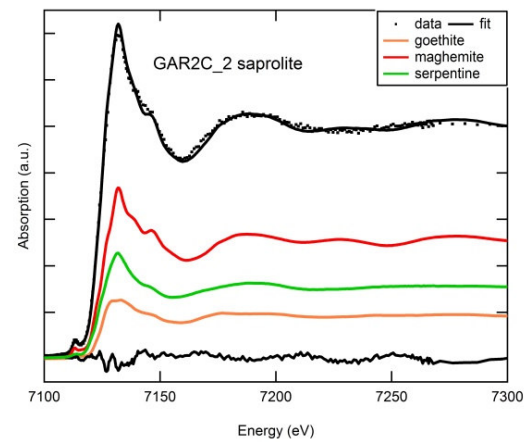
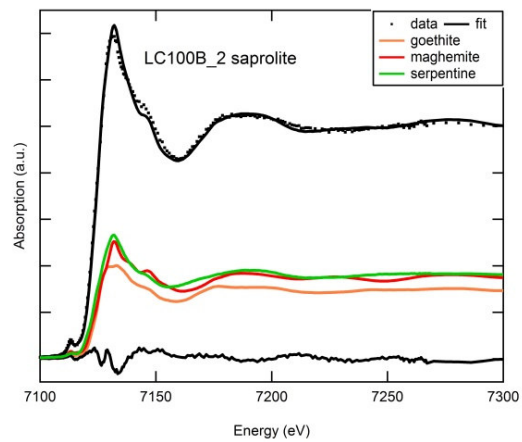
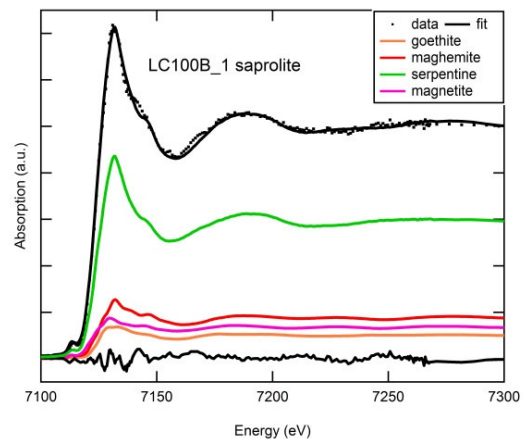
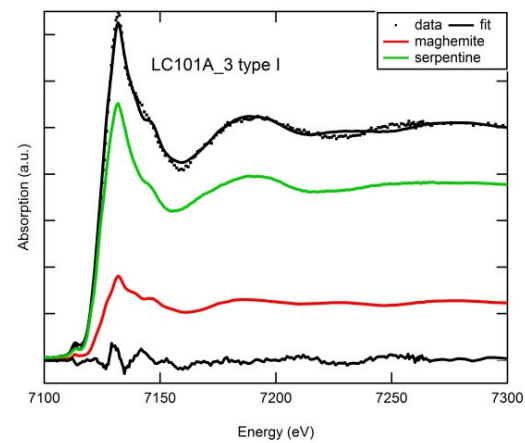
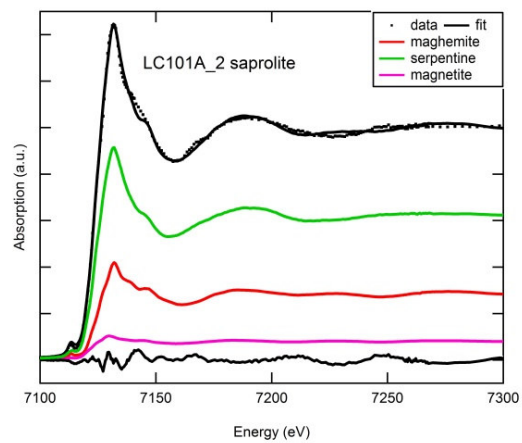
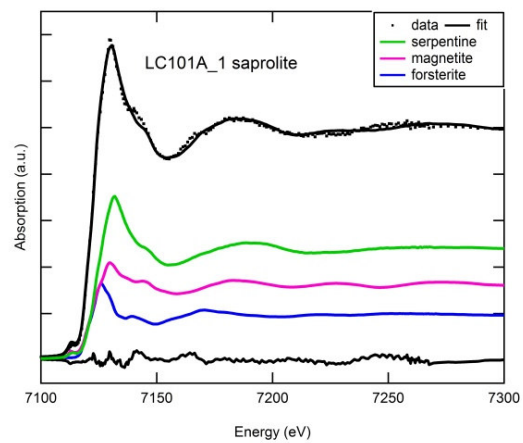


Figure 5.

ACCEPTED MANUSCRIPT

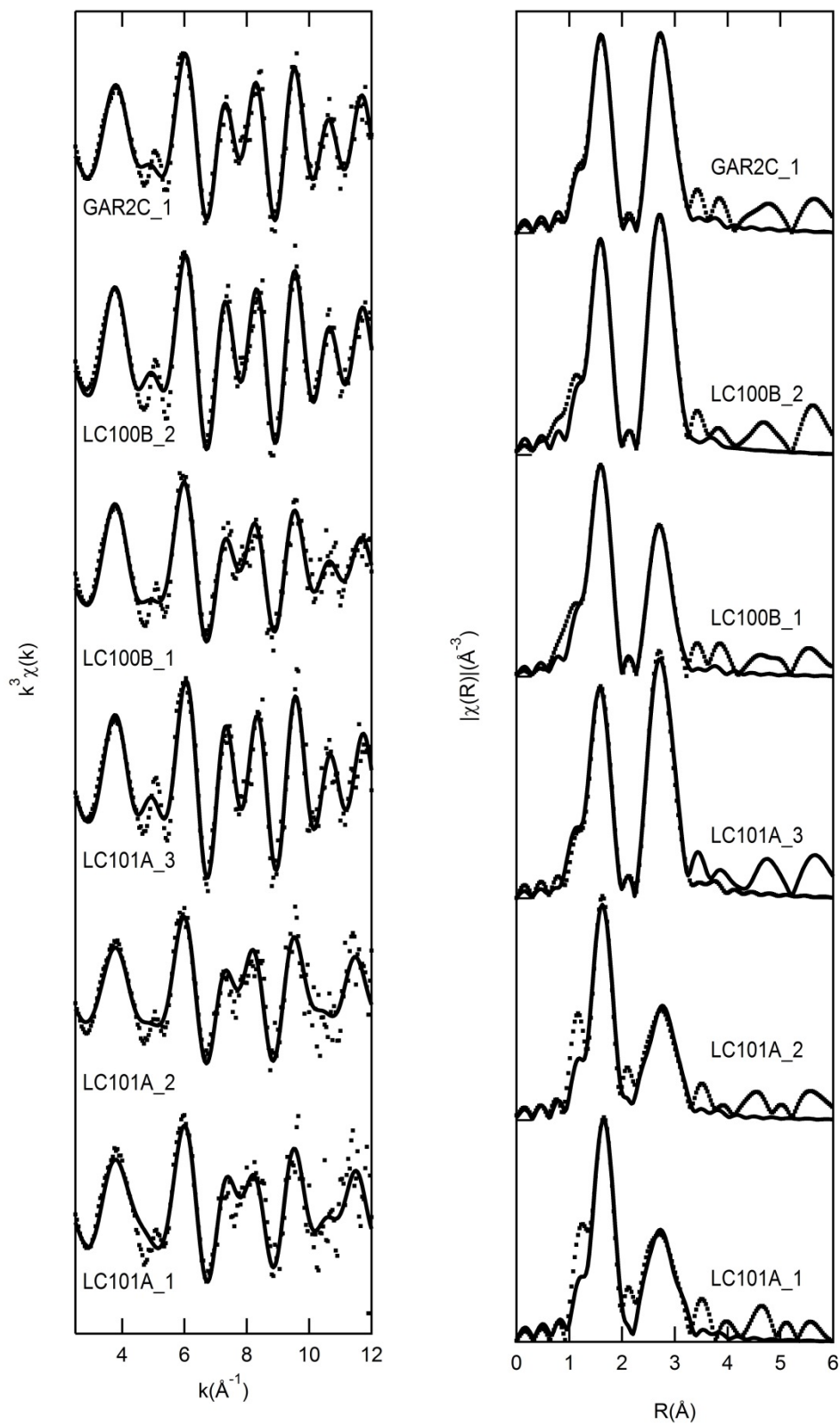


Figure 6.

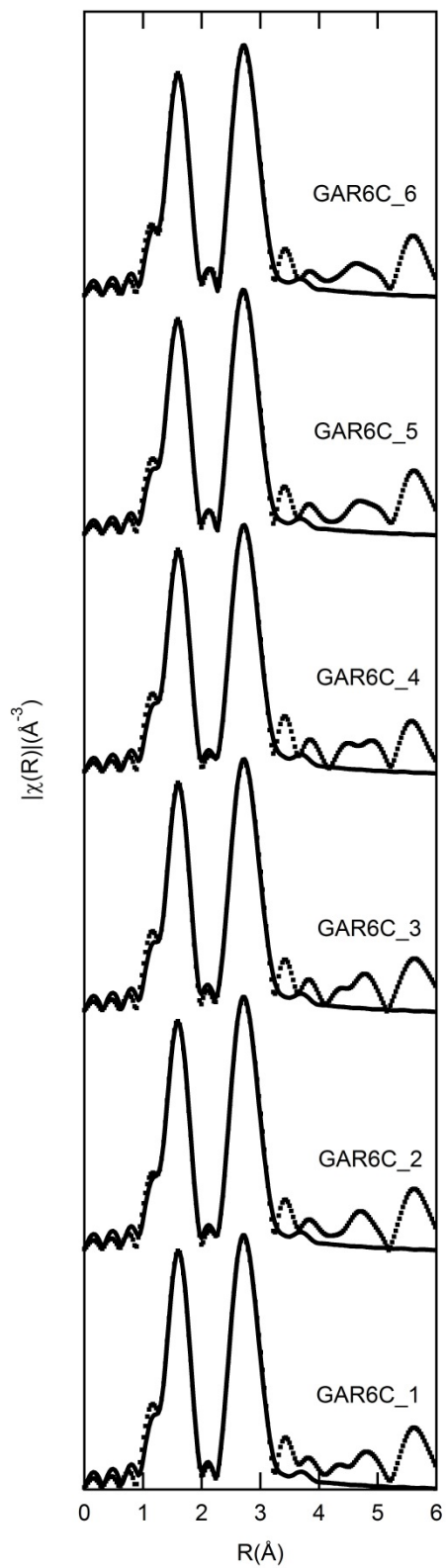
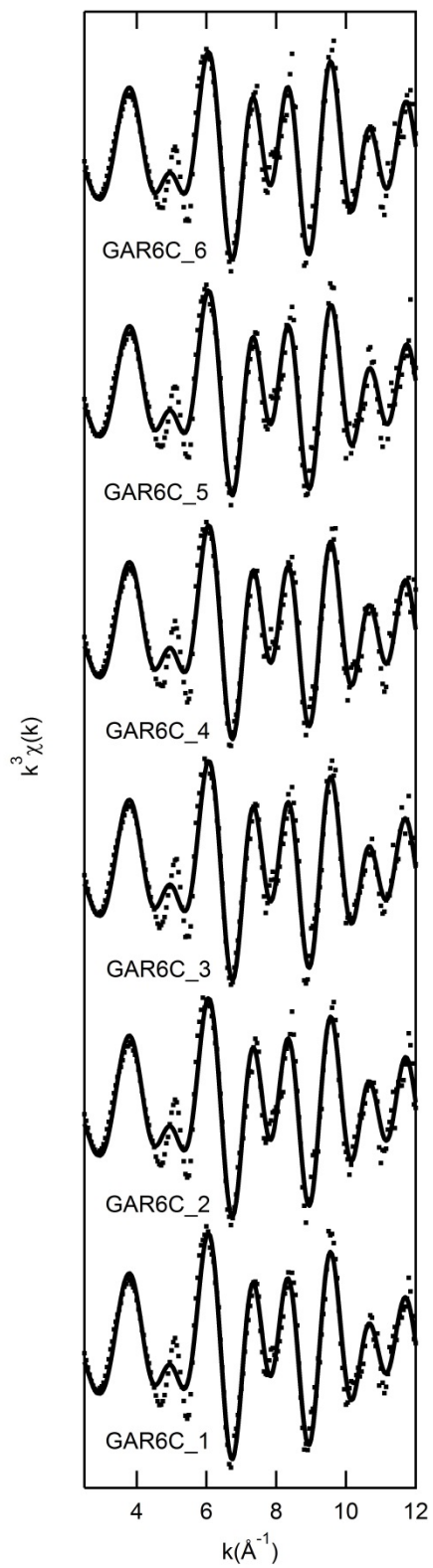


Figure 7.

ACCEPTED MANUSCRIPT

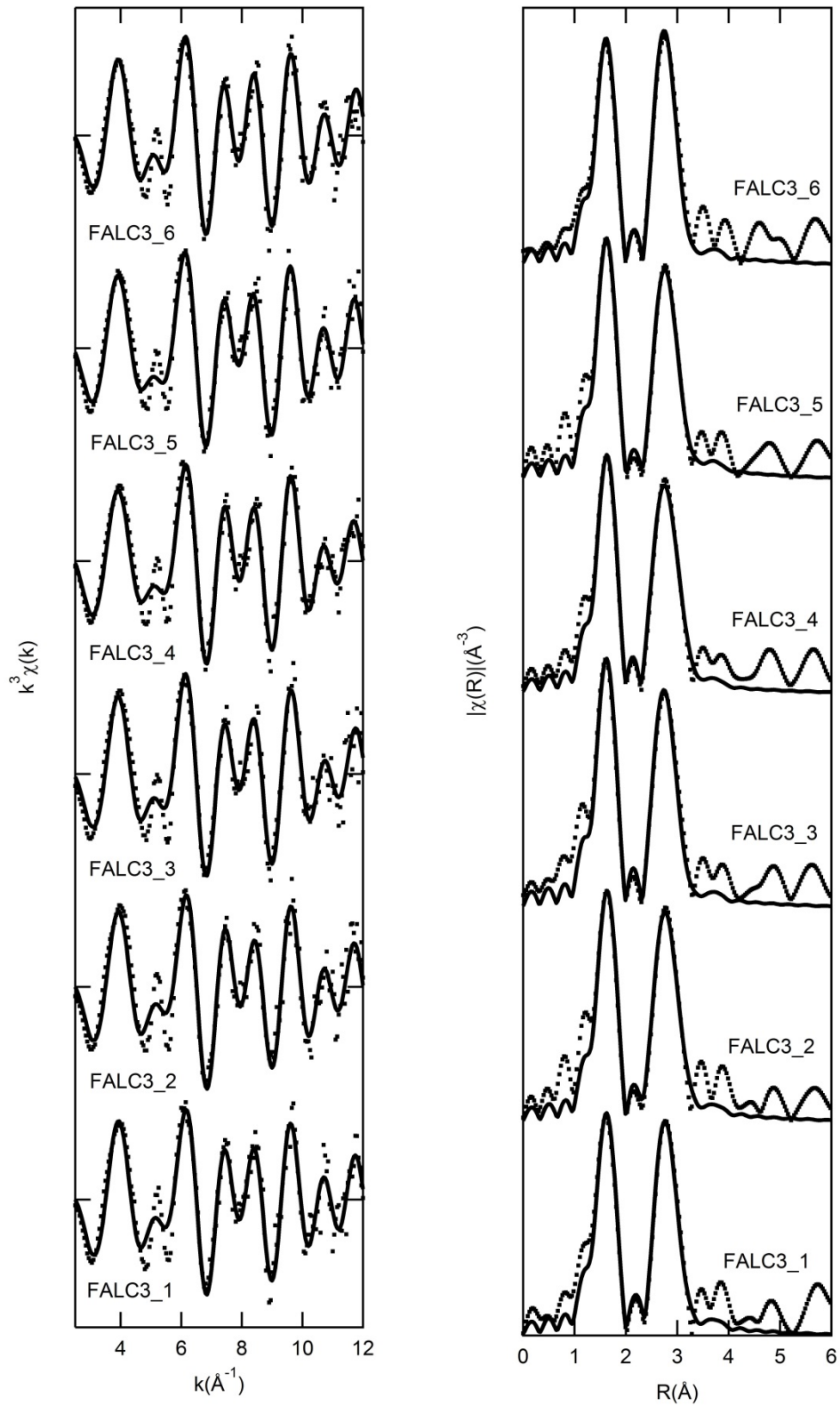


Figure 8.

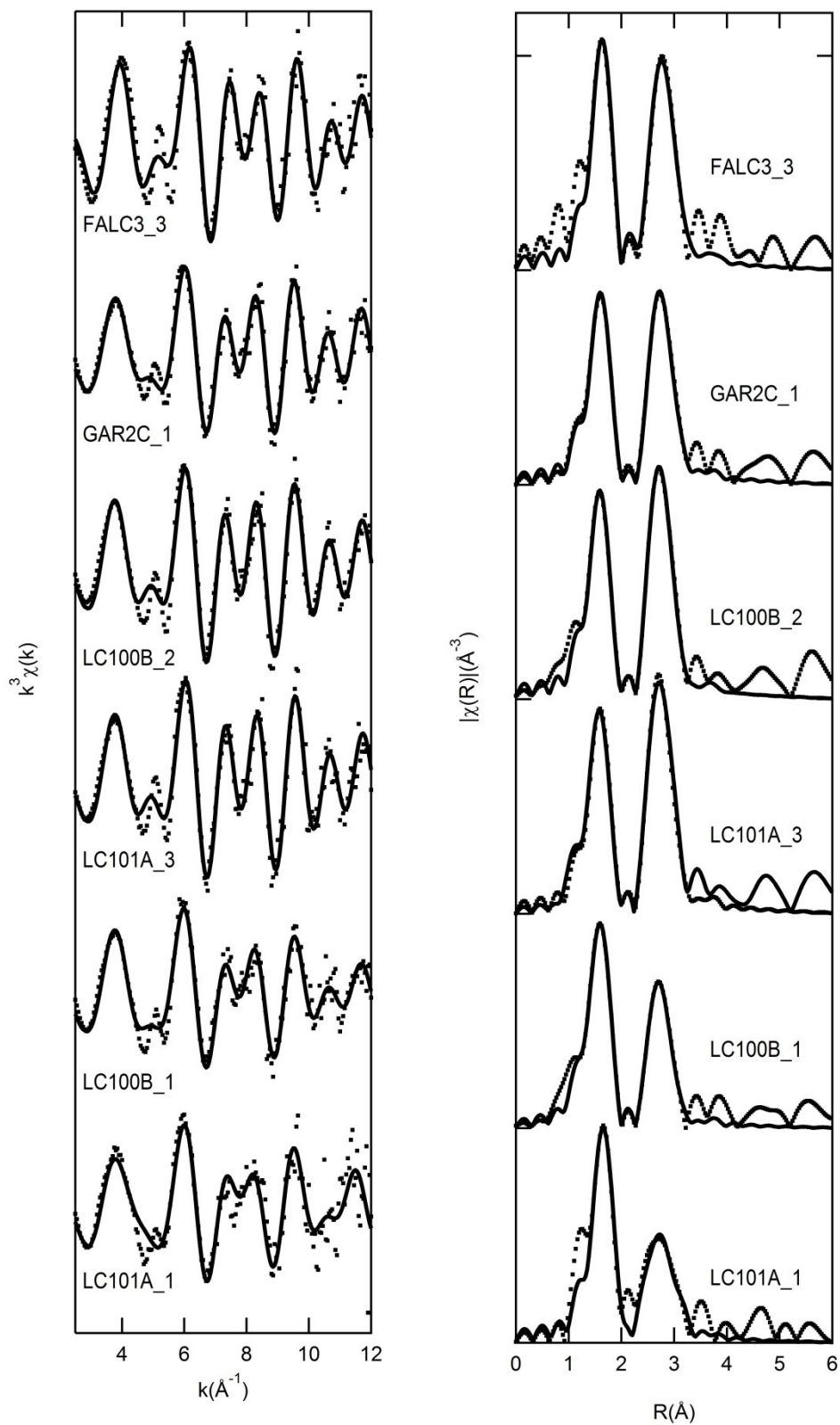


Figure 9.

Table 1. Compositions of the analyzed points obtained by EMPA in %wt. The obtained compositions have been used to classify the samples into the five garnierite types described by (Villanova-de-Benavent *et al.*, 2014).

Table 2. These are the fittings displaying the reference spectra used as standards selected from (Villanova-de-Benavent *et al.*, 2014) and the amounts of the selected references that provide the best fit for each Fe-K XANES as a weighted sum. The normalized sum—squared residual from each Fe-K XANES fit are displayed.

Table 3. Fitting values for Ni K-edge μ EXAFS on LC101A, LC100B and GAR2C. $R(\text{\AA})$ corresponds to the interatomic distances, N number of neighboring atoms, $ss2$ the Debye-Waller factor, $e0$ (eV) is the difference between the defined threshold energy and the experimentally determined threshold energy, R -factor is the fit coefficient and $RedChi2$ correspond to the goodness of fit. Errors on R and N values are usually considered around $\pm 20\%$ and $\pm 5\%$, respectively.

Table 4. Fitting values for Ni K-edge μ EXAFS on GAR6C. $R(\text{\AA})$ corresponds to the interatomic distances, N number of neighboring atoms, $ss2$ the Debye-Waller factor, $e0$ (eV) is the difference between the defined threshold energy and the experimentally determined threshold energy, R -factor is the fit coefficient and $RedChi2$ correspond to the goodness of fit. Errors on R and N values are usually considered around $\pm 20\%$ and $\pm 5\%$, respectively.

Table 5. Fitting values for Ni K-edge μ EXAFS on FALC3. $R(\text{\AA})$ corresponds to the interatomic distances, N number of neighboring atoms, $ss2$ the Debye-Waller factor, $e0$ (eV) is the difference between the defined threshold energy and the experimentally determined threshold energy, R -factor is the fit coefficient and $RedChi2$ correspond to the goodness of fit. Errors on R and N values are usually considered around $\pm 20\%$ and $\pm 5\%$, respectively.

Table 1.

Sample Type	LC-101a saprolite	LC-101a saprolite	LC-101a saprolite	LC-101a saprolite	LC-101a type I	LC-100Bb saprolite	LC-100Bb saprolite	LC-100Bb type II	LC-100Bb type II	LC-100Bb type II	GAR-3 saprolite				
SiO ₂	42.7	41.6	37.4	41.4	40.7	42.5	44.8	42.1	43.1	40.8	41.0	40.2	43.1	41.45	
TiO ₂	-	0.03	0.06	-	-	-	-	0.02	-	0.03	-	-	-	-	
Al ₂ O ₃	0.11	2.92	0.2	3.13	0.02	0.01	0.05	0.01	1.32	2.94	1.40	1.06	1.11	0.18	
Cr ₂ O ₃	-	0.93	0.09	1.11	0.12	0.03	0.04	-	0.02	-	0.02	-	0.02	0.04	
V ₂ O ₃	-	-	-	-	-	-	-	-	-	-	0.05	0.02	0.02	-	
Fe ₂ O ₃	3.90	4.65	10.60	3.36	8.91	2.66	4.91	3.05	1.92	4.92	0.66	0.46	0.60	7.54	
MnO	0.01	0.03	0.06	-	0.01	0.05	0.03	-	0.04	0.08	0.01	0.05	0.03	6.78	
ZnO	-	-	-	-	-	-	-	-	-	-	0.01	-	-	0.05	
MgO	36.8	35.3	30.8	36.7	33.4	39.6	27.6	40.4	34.7	30.1	17.7	17.6	19.1	38.29	
NiO	2.38	1.5	4.43	1.44	5.33	1.19	8.92	1.51	5.23	6.14	25.2	24.5	21.6	0.8	
CoO	-	0.02	0.02	0.02	0.03	-	-	0.02	-	-	-	-	-	-	
CaO	0.04	-	0.03	0.01	0.07	0.01	0.09	0.01	-	-	0.1	0.07	0.06	-	
Na ₂ O	-	-	-	-	-	-	-	-	-	-	-	-	-	-	
K ₂ O	0.01	0.02	-	-	0.04	-	0.06	0.01	-	-	-	-	-	-	
Sum Ox%	86.0	87.0	83.7	87.1	88.6	86.0	86.6	87.1	86.4	85.0	86.1	83.9	85.7	95.1	
O (Str Form)	7	7	7	7	7	7	7	7	7	7	7	7	7	7	
Si	2.035	1.912	1.809	2.042	1.955	2.008	2.181	1.976	2.036	1.956	2.173	2.178	2.237	1.869	
Ti	0	0.001	0.002	0	0	0	0	0.001	0	0.001	0	0	0	0	
Al	0.006	0.158	0.011	0.049	0.001	0.001	0.003	0.001	0.073	0.166	0.087	0.068	0.068	0.010	
Cr	0	0.034	0.003	0.002	0.005	0.001	0.002	0	0.001	0	0.001	0	0.001	0.001	
V	0	0	0	0	0	0	0	0	0	0	0.002	0.001	0.001	0	
Fe ³⁺	0.140	0.161	0.385	0.088	0.322	0.095	0.180	0.108	0.068	0.178	0.026	0.019	0.023	0.256	
Mn	0	0.001	0.002	0.001	0	0.002	0.001	0	0.002	0.003	0	0.002	0.001	0.002	
Zn	0	0	0	0	0	0	0	0	0	0	0	0	0	0	
Mg	2.62	2.43	2.22	2.54	2.39	2.79	2.01	2.83	2.44	2.15	1.40	1.42	1.48	2.57	
Ni	0.091	0.056	0.172	0.170	0.206	0.045	0.349	0.057	0.199	0.237	1.08	1.07	0.904	0.029	
Co	0	0.001	0.001	0	0.001	0	0	0.001	0	0	0	0	0	0	
Ca	0.002	0	0.002	0	0.004	0.001	0.005	0.001	0	0	0.006	0.004	0.003	0	
Na	0	0	0	0	0	0	0	0	0	0	0	0	0	0	
K	0.001	0.001	0	0	0.002	0	0.004	0.001	0	0	0	0	0	0	
Σcations	4.89	4.75	4.60	4.89	4.88	4.94	4.73	4.97	4.82	4.69	4.77	4.76	4.72	4.74	
XTlc (*)	-	-	-	-	0.008	0.113	0.293	0.009	-	-	0.359	0.365	0.439	-	

Table 1 (Continued)

Sample Type	GAR-3 saprolite	GAR-3 type III	GAR-3 type III	GAR-3 type III	GAR-3 type III	GAR-6 type IV	GAR-6 type IV	GAR-6 type IV	GAR-6 type IV	FALC-3 sep-falc	FALC-3 sep-falc	FALC-3 sep-falc	FALC-3 sep-falc
SiO ₂	45.1	43.1	44.8	39.4	39.5	45.6	46.6	51.0	47.3	52.3	47.6	49.6	49.60
TiO ₂	0.02	0.03	-	-	0.02	-	0.03	0.01	0.01	-	-	-	0.03
Al ₂ O ₃	0.06	0.09	0.03	-	0.02	0.08	0.15	0.14	0.13	0.53	0.33	0.31	0.50
Cr ₂ O ₃	-	0.03	0.05	0.04	0.04	0.02	0.02	0.03	-	0.02	-	0.00	0.02
V ₂ O ₃	-	-	-	-	-	-	-	0.04	-	-	-	-	-
Fe ₂ O ₃	1.923	0.834	0.20	0.067	0.122	0.011	0.067	-	-	0.089	0.044	0.089	0.033
MnO	1.73	-	-	0.00	-	0.02	-	-	-	0.01	0.06	0.02	0.02
ZnO	0.02	-	-	-	-	0.05	0.06	-	-	-	-	-	-
MgO	40.8	11.5	11.0	7.57	6.88	7.99	9.42	14.7	8.7	14.9	9.5	10.8	10.64
NiO	0.32	29.1	33.2	37.6	41.1	31.8	29.9	24.3	31.4	12.3	26.8	23.4	18.26
CoO	-	-	-	-	-	-	-	-	-	-	-	-	-
CaO	-	-	-	-	-	0.04	0.09	0.04	0.06	-	-	-	-
Na ₂ O	-	0.04	-	0.01	-	-	-	-	-	-	0.06	0.04	0.03
K ₂ O	-	-	0.02	0.02	-	-	-	-	-	-	0.06	0.10	-
Sum Ox%	89.9	84.7	89.3	84.7	87.7	85.6	86.3	90.2	87.5	80.0	84.5	84.3	79.13
O (Str Form)	7	7	7	7	7	11	11	11	11	32	32	32	32
Si	2.04	2.36	2.36	2.29	2.26	3.89	3.89	3.90	3.91	12.2	11.6	11.8	12.1
Ti	0.001	0.001	0	0	0.001	0	0.002	0.001	0.001	0	0	0	0.006
Al	0.003	0.006	0.002	0	0.001	0.008	0.015	0.013	0.013	0.145	0.094	0.087	0.144
Cr	0	0.001	0.002	0.002	0.002	0.001	0.001	0.002	0	0.004	0	0	0.004
V	0	0	0	0	0	0	0	0.002	0	0	0	0	0
Fe ³⁺	0.065	0.034	0.008	0.003	0.005	0.001	0.004	0	0	0.016	0.008	0.016	0.006
Mn	0.001	0	0	0	0	0.001	0	0	0	0.002	0.012	0.004	0.004
Zn	0	0	0	0	0	0.003	0.004	0	0	0	0	0	0
Mg	2.75	0.94	0.86	0.66	0.59	1.02	1.17	1.67	1.07	5.15	3.42	3.82	3.88
Ni	0.012	1.28	1.41	1.76	1.89	2.18	2.01	1.49	2.09	2.29	5.24	4.46	3.59
Co	0	0	0	0	0	0	0	0	0	0	0	0	0
Ca	0	0	0	0	0	0.004	0.008	0.003	0.005	0	0	0	0
Na	0	0.004	0	0.001	0	0	0	0	0	0	0.028	0.018	0.014
K	0	0	0.001	0.001	0	0	0	0	0	0	0.019	0.030	0
Σcations	4.86	4.62	4.62	4.71	4.74	7.10	7.10	7.09	7.08	19.75	20.40	20.21	19.79
X _{Tlc} (*)	-	0.575	0.557	0.424	0.369	0.829	0.838	0.860	0.866	1.48	1.02	1.14	1.466

Table 2.

Sample	LC101A_1	LC101A_2	LC101A_3	LC100B_1	LC100B_2	GAR2C_2
Type	saprolite	saprolite	Type I	saprolite	saprolite	saprolite
Forsterite(%)	20	-	-	-	-	-
Magnetite (%)	33	10	-	14	-	-
Serpentine(%)	48	66	77	59	36	31
Maghemite(%)	-	24	23	18	35	51
Goethite(%)	-	-	-	10	30	18
Norm. Sum. Sq. Res.	1.59E-04	1.86E-04	3.06E-04	2.57E-04	3.38E-04	2.76E-4

Table 3.

	Ni-O	Ni-Mg	Ni-Ni	Ni-Si	e0	R-factor	RedChi2
LC101A_1							
R(Å)	2.08	3	-	3.3	1.23	3.3E-2	9.22
N	4.6	4.6	-	3.1			
Ss2	0.004	0.01	-	0.004			
LC101A_2							
R(Å)	2.06	3.06	3.06	3.3	-3.46	2E-2	8.12
N	4.2	3.1	2.9	2.8			
Ss2	0.003	0.011	0.011	0.003			
LC101A_3							
R(Å)	2.06	-	3.04	3.17	-3.28	4.1E-3	6.09
N	5.2	-	5.2	3.8			
Ss2	0.006	-	0.007	0.007			
LC100B_1							
R(Å)	2.06	3.08	3.08	3.17	-3.46	2E-2	8.12
N	5.8	0.3	5.7	3.9			
Ss2	0.007	0.009	0.009	0.007			
LC100B_2							
R(Å)	2.06	-	3.08	3.21	-3.39	1E-3	8.28
N	4.8	-	5.22	4.24			
Ss2	0.006	-	0.006	0.006			
GAR2C_1							
R(Å)	2.06	-	3.08	3.24	-2.45	1E-3	3.98
N	4.8	-	3.72	2.04			
Ss2	0.006	-	0.006	0.007			

Table 4.

	Ni-O	Ni-Ni	Ni-Si	e0	R-factor	RedChi2
GAR6C_1						
R(Å)	2.06	3.08	3.24	-0.05	2E-2	7.47
N	5.12	5.05	3.2			
Ss2	0.005	0.006	0.007			
GAR6C_2						
R(Å)	2.06	3.08	3.24	-3.46	2E-2	8.12
N	5.04	4.68	3.36			
Ss2	0.006	0.005	0.007			
GAR6C_3						
R(Å)	2.06	3.08	3.25	-3.28	4.1E-3	6.09
N	4.68	4.68	3.36			
Ss2	0.005	0.004	0.008			
GAR6C_4						
R(Å)	2.06	3.08	3.24	-4.63	1E-3	1.27
N	5.04	4.68	3.4			
Ss2	0.006	0.005	0.007			
GAR6C_5						
R(Å)	2.05	3.07	3.21	-3.39	1E-3	8.28
N	4.56	4.99	3.99			
Ss2	0.005	0.006	0.009			
GAR6C_6						
R(Å)	2.06	3.07	3.23	-2.45	1E-3	3.98
N	4.56	4.08	3.88			
Ss2	0.005	0.006	0.008			

Table 5.

Falc3_1	Ni-O	Ni-Ni	Ni-Si	e0	R-factor	RedChi2
R(Å)	2.06	3.09	3.23	1.69	4.8E-3	8.42
N	5.34	3.04	5.08			
Ss2	0.006	0.006	0.006			
Falc3_2	Ni-O	Ni-Ni	Ni-Si	e0	R-factor	RedChi2
R(Å)	2.07	3.07	3.26	2.34	4.6E-3	8.79
N	5.1	2.82	3.72			
Ss2	0.005	0.007	0.003			
Falc3_3	Ni-O	Ni-Ni	Ni-Si	e0	R-factor	RedChi2
R(Å)	2.06	3.07	3.24	1.17	5.1E-3	7.15
N	5.34	3.6	3.56			
Ss2	0.005	0.007	0.004			
Falc3_4	Ni-O	Ni-Ni	Ni-Si	e0	R-factor	RedChi2
R(Å)	2.06	3.07	3.26	1.88	3.6E-3	17.8
N	5.04	3.18	3.36			
Ss2	0.005	0.006	0.004			
Falc3_5	Ni-O	Ni-Ni	Ni-Si	e0	R-factor	RedChi2
R(Å)	2.05	3.08	3.25	1.54	2.7E-3	8.51
N	5.52	3.48	2.72			
Ss2	0.005	0.007	0.002			
Falc3_6	Ni-O	Ni-Ni	Ni-Si	e0	R-factor	RedChi2
R(Å)	2.06	3.08	3.2	1.43	7.2E-3	20.05
N	5.1	5.1	3.44			
Ss2	0.005	0.007	0.005			